The Asian–Australian Monsoon and El Niño–Southern Oscillation in the NCAR Climate System Model*

Gerald A. Meehl and Julie M. Arblaster

National Center for Atmospheric Research,+ Boulder, Colorado

(Manuscript received 2 April 1997, in final form 23 June 1997)

ABSTRACT

Features associated with the Asian–Australian monsoon system and El Niño–Southern Oscillation (ENSO) are described in the National Center for Atmospheric Research (NCAR) global coupled Climate System Model (CSM). Simulation characteristics are compared with a version of the atmospheric component of the CSM, the NCAR CCM3, run with time-evolving SSTs from 1950 to 1994, and with observations. The CSM is shown to represent most major features of the monsoon system in terms of mean climatology, interannual variability, and connections to the tropical Pacific. This includes a representation of the Southern Oscillation links between strong Asian–Australian monsoons and associated negative SST anomalies in the eastern equatorial Pacific. The equatorial SST gradient across the Pacific in the CSM is shown to be similar to the observed with somewhat cooler mean SSTs across the entire Pacific by about 1°–2°C. The seasonal cycle of SSTs in the eastern equatorial Pacific has the characteristic signature seen in the observations of relatively warmer SSTs propagating westward in the first half of the year followed by the reestablishment of the cold tongue with relatively colder SSTs propagating westward in the second half of the year. Like other global coupled models, the propagation is similar to the observed but with the establishment of the relatively warmer water in the first half of the year occurring about 1–2 months later than observed. The seasonal cycle of precipitation in the tropical eastern Pacific is also similar to other global coupled models in that there is a tendency for a stronger-than-observed double ITCZ year round, particularly in northern spring, but with a well-reproduced annual maximum of ITCZ strength north of the equator in the second half of the year. Time series of area-averaged SSTs for the NINO3 region in the eastern equatorial Pacific show that the CSM is producing about 60% of the amplitude of the observed variability in that region, consistent with most other global coupled models. Global correlations between NINO3 time series, global surface temperatures, and sea level pressure (SLP) show that the CSM qualitatively reproduces the major spatial patterns associated with the Southern Oscillation (lower SLP in the central and eastern tropical Pacific when NINO3 SSTs are relatively warmer and higher SLP over the far western Pacific and Indian Oceans, with colder water in the northwest and southwest Pacific). Indices of Asian–Australian monsoon strength are negatively correlated with NINO3 SSTs as in the observations. Spectra of time series of Indian monsoon, Australian monsoon, and NINO3 SST indices from the CSM show amplitude peaks in the Southern Oscillation and tropospheric biennial oscillation frequencies (3–6 yr and about 2.3 yr, respectively) as observed. Lag correlations between the NINO3 SST index and upper-ocean heat content along the equator show eastward propagation of heat content anomalies with a phase speed of about 0.3 m s^{-1}, compared to observed values of roughly 0.2 m s^{-1}. Composites of El Niño (La Niña) events in the CSM show similar seasonal evolution to composites of observed events with warming (cooling) of greater than several tenths of a degree beginning early in northern spring of year 0 and diminishing around northern spring of year +1, but with a secondary resurgence in the CSM events later in northern spring of year +1. The CSM also shows the largest amplitude ENSO SST and low-level wind anomalies in the western tropical Pacific, with enhanced interannual variability of SSTs extending northeastward and southeastward toward the subtropics, compared to largest interannual SST variability in the central and eastern tropical Pacific in the observations.

Corresponding author address: Dr. Gerald A. Meehl, Climate and Global Dynamics Division, National Center for Atmospheric Research, P.O. Box 3000, Boulder, CO 80307-3000.
E-mail: meehl@ncar.ucar.edu

1. Introduction

Though atmospheric general circulation models (GCMs) can simulate many aspects of interannual variability associated with the Asian–Australian monsoons and ENSO when run with observed SSTs (e.g., Kitoh 1992; Palmer et al. 1992; Sperber and Palmer 1996), global coupled general circulation models have also been shown to perform reasonably well in simulating such features of the mean climate and climate variability

JJA
Long—term Average
Precipitation and 850 hPa Winds

a)   Observed

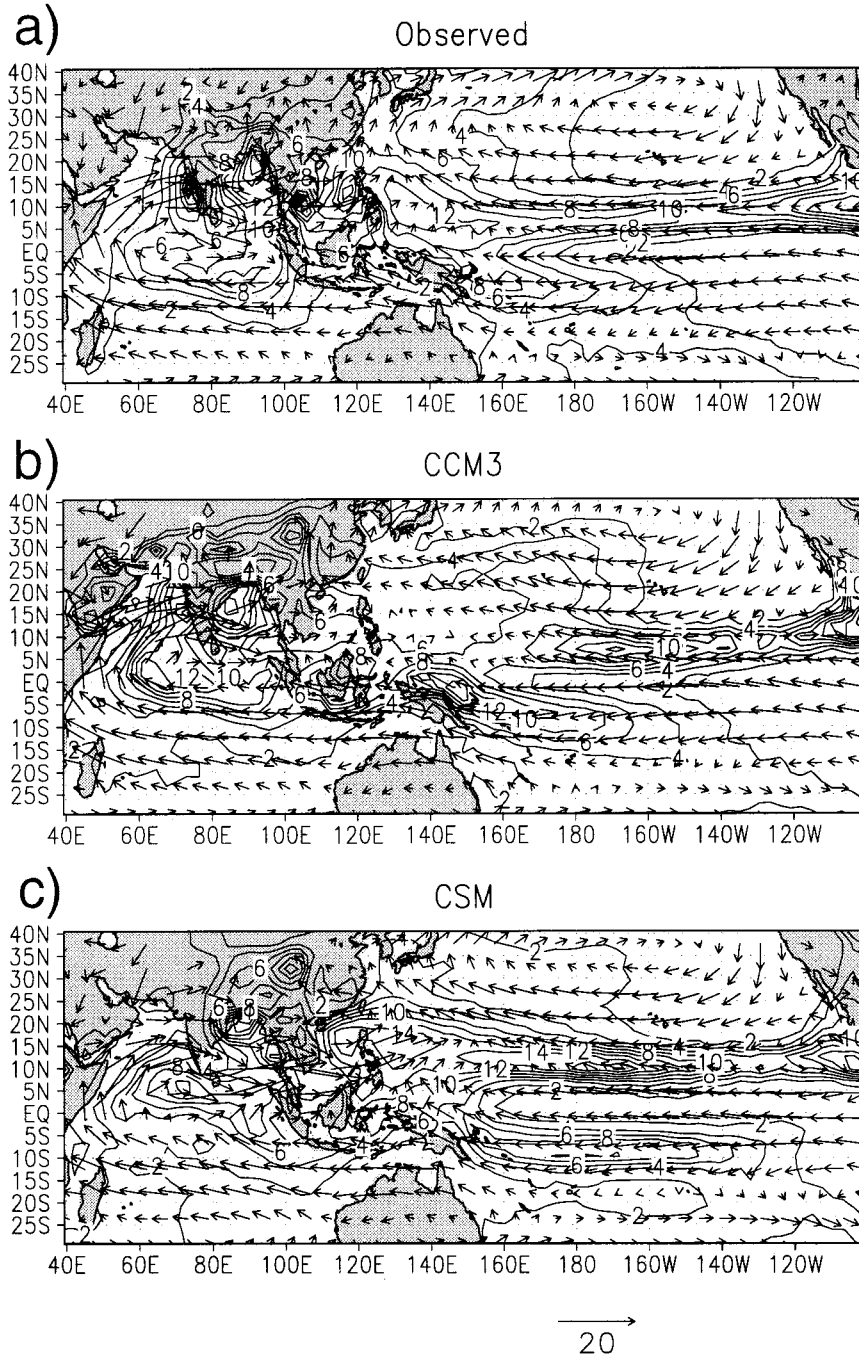b)   CCM3

c)   CSM

FIG. 1. JJA average precipitation (mm day^{-1}) and 850-mb wind vectors (scale vector at bottom in m s^{-1}) (a) observed from the NCAR–NCEP reanalyses for winds, and Xie and Arkin (1996) for precipitation, 1979–95, (b) 45-yr average (1950–94) for the CCM3 run with the observed time-evolving SSTs, (c) 45-yr average from the CSM.

JJA
Long–term Average
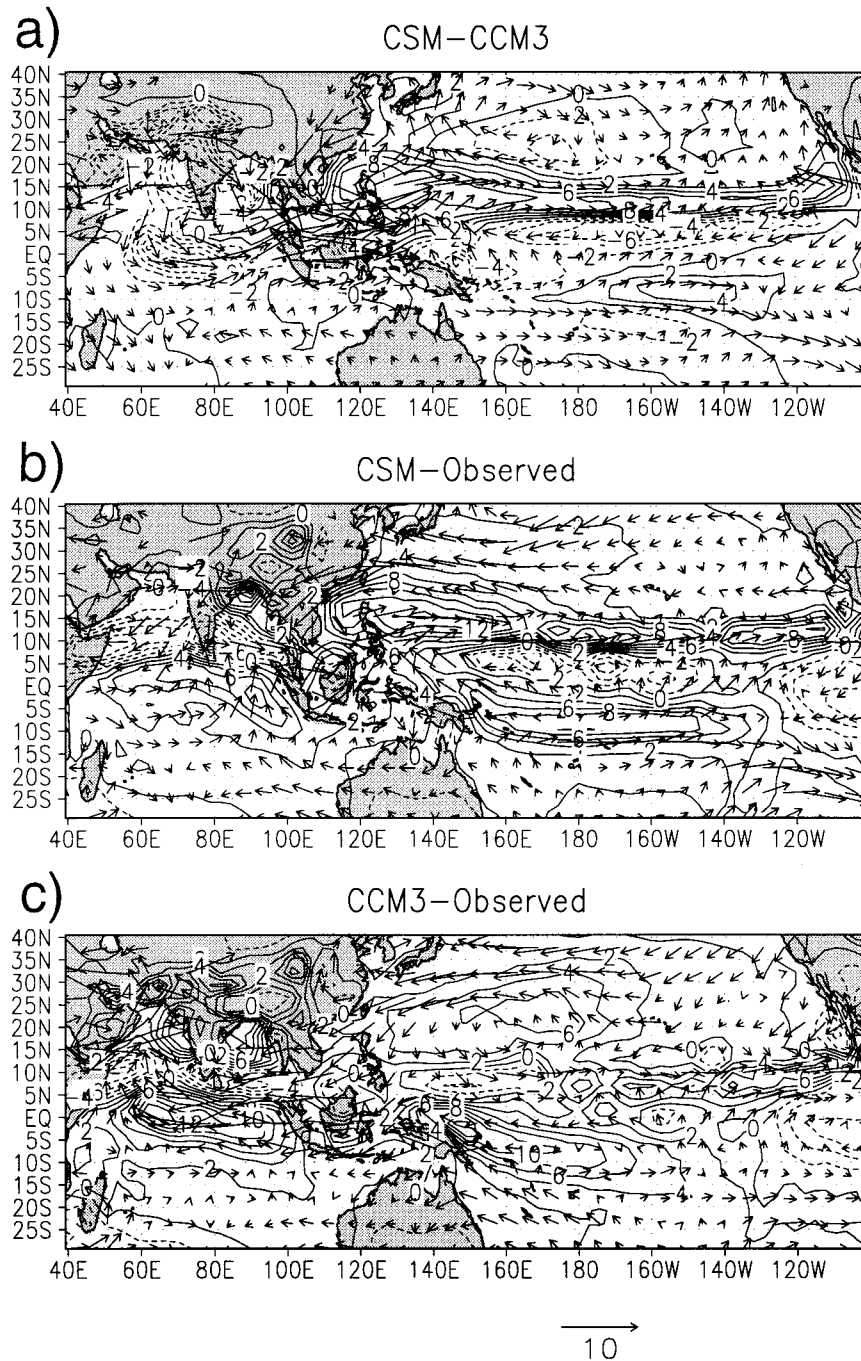## Precipitation and 850 mb Winds

FIG. 2. (a) Precipitation and 850-mb wind vector differences, JJA, 45-yr averages for CSM minus CCM3; (b) same as (a) except for CSM minus observations [NCAR–NCEP reanalyses for winds, Xie and Arkin (1996) for precipitation]; (c) same as (b) except for CCM3 − observations; (d) JJA sea surface temperature differences, CSM − observations from the NCAR–NCEP reanalysis period from 1979 to 1995; (e) JJA latent heat flux differences, 45-yr averages, CSM − CCM3.

JJA
Long-term Average

d)

Sea Surface Temperature
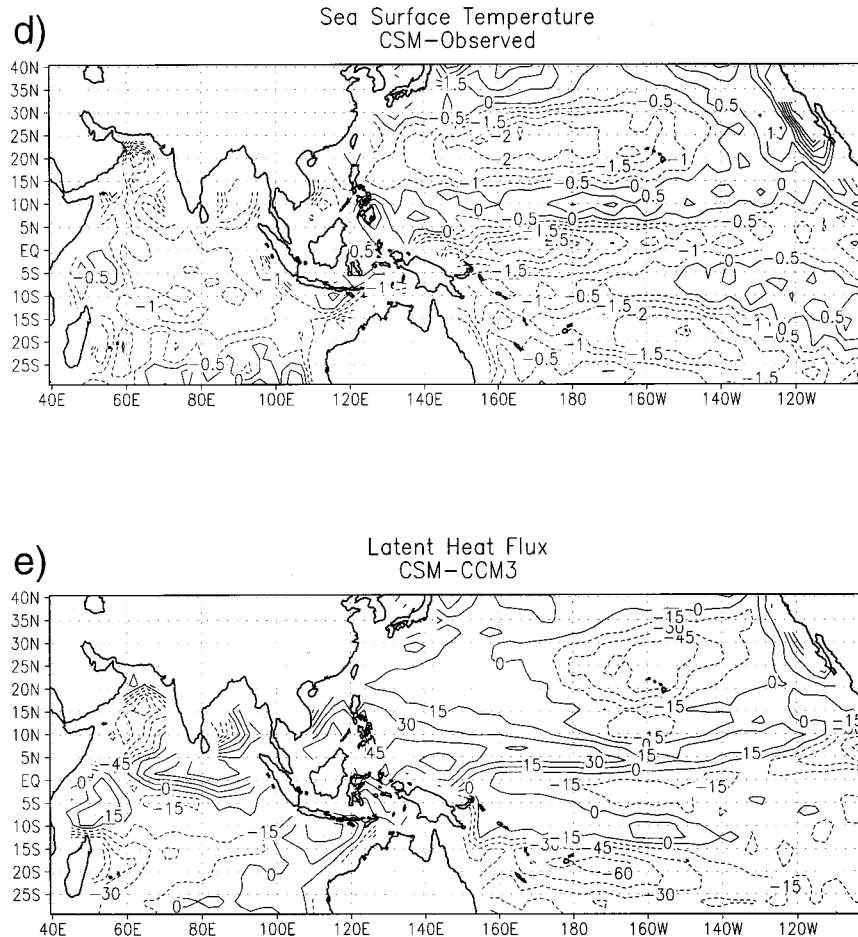CSM—Observed

Latent Heat Flux
CSM—CCM3

e)

FIG. 2. (*Continued*)

in those regions (IPCC 1996). The Asian–Australian monsoon system, with its profound linkages to not only regional but global climate (e.g., Nicholls 1984; Krishnamurti et al. 1989, 1990; Yasunari and Seki 1992; Ju and Slingo 1995), has been studied in global coupled models to gain insights into mechanisms of interannual variability (Latif et al. 1994; Meehl 1994, 1997a) and for changes in mean monsoon conditions and alterations in interannual variability due to an increase of CO_2 (Meehl and Washington 1993; Chakraborty and Lal 1994; Lal et al. 1994). Coarse-grid coupled models have been documented to reproduce "ENSO-like" interannual variability but with about half the observed amplitude (Meehl 1990; Lau et al. 1992; Nagai et al. 1992; Tett 1995). More recent global coupled model versions with improved latitudinal resolution in the equatorial Tropics have shown somewhat higher amplitude SST variability in the eastern equatorial Pacific (Yukimoto et al. 1996; Roeckner et al. 1996). Changes in ENSO

effects in such models have also been studied in relation to increased CO_2 (Meehl et al. 1993a; Knutson and Manabe 1994; Tett 1995; Knutson et al. 1997).

In general, coupled models without flux adjustment have had difficulties simulating the seasonal cycle in the eastern tropical Pacific (Mechoso et al. 1995). Though first-order characteristics of tropical interannual variability have been represented in global coupled models (Meehl et al. 1994; Meehl 1995; Knutson et al. 1997), there have been deficiencies in some of the patterns of the simulated interannual variability in the Tropics associated with monsoon–ENSO relationships (Meehl et al. 1993a).

The purpose of this paper is to describe general characteristics of the mean climatology, seasonal cycle, interannual variability, and patterns of variability of Asian–Australian monsoon and ENSO in the National Center for Atmospheric Research (NCAR) Climate System Model (CSM). Since the dynamical coupling of the

component models can significantly alter the simulation from that in the components alone (Meehl 1997b), the results from the CSM will be compared to a simulation with the atmospheric model (the NCAR Community Climate Model vesion 3) run with time-evolving observed SSTs from 1950 to 1994 (simply termed "CCM3" here). This comparison will demonstrate areas where the coupled model simulation has been changed due to coupling with interactive ocean and sea ice components. Both the uncoupled and coupled models will be compared to observations—the NCAR–NCEP (National Centers for Environmental Prediction, formerly the National Meteorological Center) reanalyses from 1973 to 1995 and the Xie and Arkin (1996) precipitation dataset—to assess their performance.

2. Model description and climatology

The NCAR CSM is a global coupled ocean–atmosphere–sea ice–land surface model. Model details are given elsewhere in this issue. Briefly, the atmospheric GCM is the NCAR CCM3 with T42 resolution (an equivalent grid spacing of roughly $2.5° \times 2.5°$) and 18 levels (hybrid coordinates; see details and references in Kiehl et al. 1998). Following Laprise (1992), a coupled model with this spatial resolution can probably resolve features closer to $4° \times 4°$ or $5° \times 5°$. The ocean is a global GCM with nominal $2.4° \times 2.4°$ grid spacing reduced to $1.2°$ latitude in the equatorial Tropics, with 45 levels in the vertical. The ocean GCM includes the Gent–McWilliams mixing scheme, a K-profile parameterization mixed layer, and an upstream differencing scheme (see details and references in Gent et al. 1998). The sea ice is adapted from a previous version of a global coupled model at NCAR (Meehl and Washington 1995; Washington and Meehl 1996). It has Semtner-3-layer thermodynamics and a version of the Flato–Hibler ice dynamics (see Weatherly et al. 1998 for more complete description and references). The land surface is the land surface model (LSM) with specified vegetation types and many surface processes (see Bonan 1998).

The ocean is spun up with an accelerated deep ocean, first with observations, and then with repeated forcing from 5 yr of an atmospheric model integration (for more details see Boville and Gent 1998). No flux adjustments are used and the resulting coupled surface climate simulation is stable (no large trends in surface variables) on the multicentury timescale. A 45-yr period relatively early in the integration (years 16–60) is analyzed here, but the stability of the model indicates that these results are also representative of other periods in the coupled integration.

The model climatology of precipitation and 850-mb winds in the monsoon–Pacific region is shown for June–August (JJA) in Fig. 1 for the CSM compared to the CCM3 and observations. Most regional precipitation features are qualitatively represented in both the

CCM3 and CSM compared to observations with a south Asian monsoon precipitation maximum, ITCZ rainfall in the equatorial Indian and Pacific Ocean north of the equator, and South Pacific convergence zone (SPCZ) rainfall in the southwestern Pacific (Figs. 1a–c). The CCM3 (Fig. 1b) has a precipitation distribution over the Indian region that more closely resembles the observations (Fig. 1a) than the CSM (Fig. 1c), particularly over the west coast and northwestern regions of India. The cross-equatorial low-level flow is well represented in both the CCM3 and CSM simulations with strong southwesterly inflow into south Asia from across the Arabian Sea and Bay of Bengal. The CSM has more of a zonally oriented SPCZ in the southwestern Pacific than the observations or the CCM3.

A maximum of precipitation near the Philippines that was somewhat deficient in CCM3 (Fig. 2c) is reestablished with a larger amplitude than the observations in the CSM (Figs. 2a,b). Precipitation and 850-mb vector wind differences in Fig. 2 show that the CSM low-level inflow into the Indian monsoon region is weaker than the CCM3 (easterly and northeasterly wind vector anomalies over the Arabian Sea in Fig. 2a) in association with the reduced monsoon rainfall over the Indian region in the CSM (Fig. 2a). Since the CCM3 simulates greater than observed precipitation amounts by about 6–9 mm day^{-1} in most of the regional precipitation centers (Indian monsoon, Pacific ITCZ, and SPCZ; Fig. 2c), the CSM reflects many of those same magnitude errors but with less positive precipitation anomaly areas over most of India (as suggested in Fig. 2a) and the additional positive precipitation anomaly near the Philippines (Fig. 2b). Anomalous low-level convergence into this Philippine precipitation maximum is evident by comparing the low-level wind vector differences in the CSM compared to the CCM3 (Fig. 2a). The 200-mb wind anomalies (not shown) are consistent with the low-level anomalies in that the tropical easterly jet over India is weaker in the CSM compared to the CCM3 and observations.

The precipitation errors in the CSM are related to SST errors simulated in the coupled model (Fig. 2d) with a band of anomalously warm SSTs with values of about 1°C near 10°N in the Pacific. These SST anomalies, along with the low-level wind anomalies in Fig. 2a, are related to changes in latent heat flux between the CCM3 and CSM. There is anomalously high latent heat flux (i.e., greater evaporation) with anomalies of greater than 30 W m^{-2} south of India, in the Pacific ITCZ region, in the western Pacific near the Philippines, and in a zonally oriented band near the SPCZ (Fig. 2e). There are zonally oriented anomalously warm SSTs near 10°S with greatest positive anomalies east of 150°W in the CSM. This type of error is a common one in coupled models (Mechoso et al. 1995) and could be related in part to inadequate simulation of stratus clouds off the west coast of South America (Ma et al. 1996). The anomalies in the regional pre-

DJF
Long–term Average
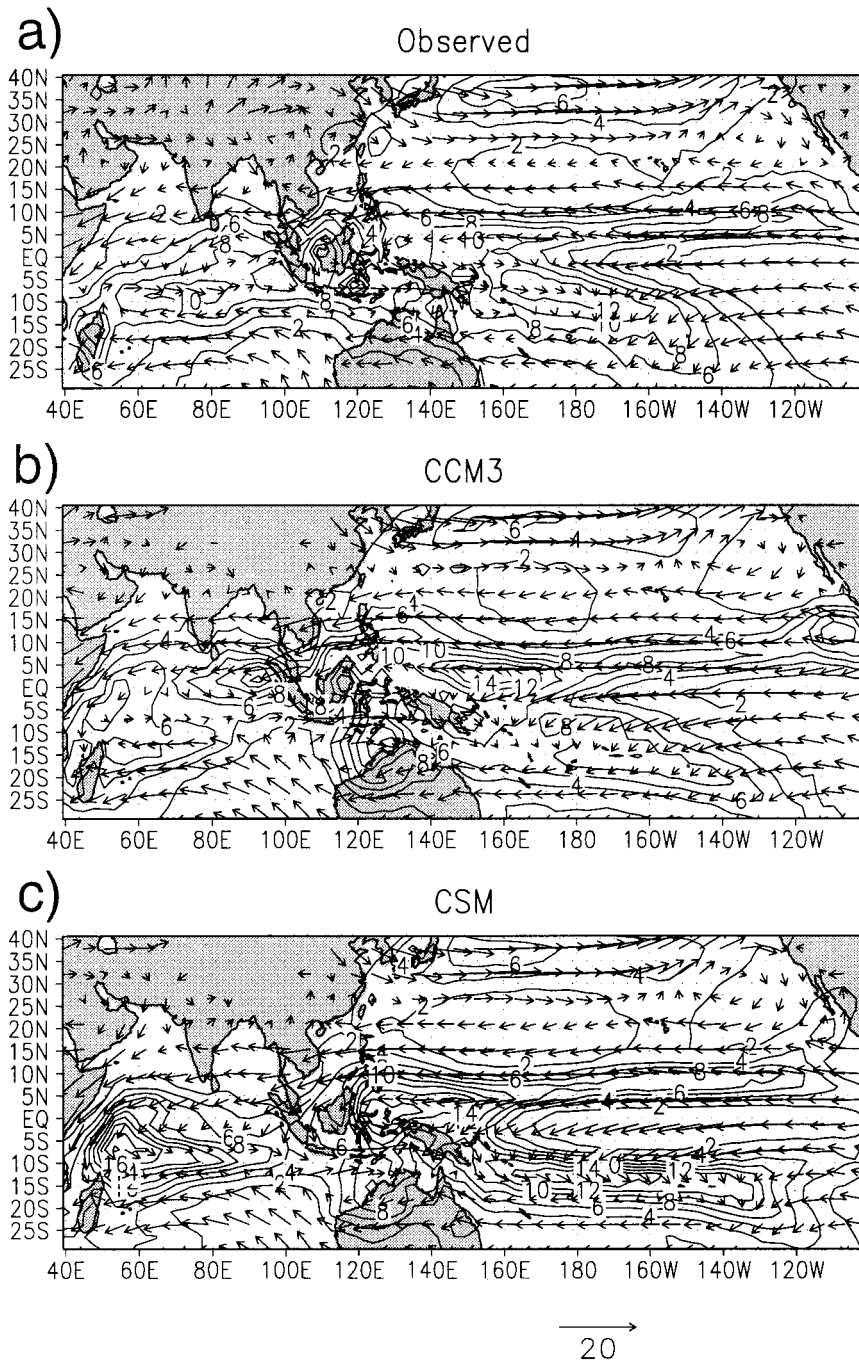## Precipitation and 850 hPa Winds

FIG. 3. DJF average precipitation (mm day^{-1}) and 850-mb wind vectors (scale vector at bottom in m s^{-1}) (a) observed from the NCAR–NCEP reanalyses for winds, and Xie and Arkin (1996) for precipitation, 1979–95; (b) 45-yr average (1950–94) for the CCM3 run with the observed time-evolving SSTs; (c) 45-yr average from the CSM.

DJF
Long-term Average
Precipitation and 850 mb Winds

a) CSM-CCM3

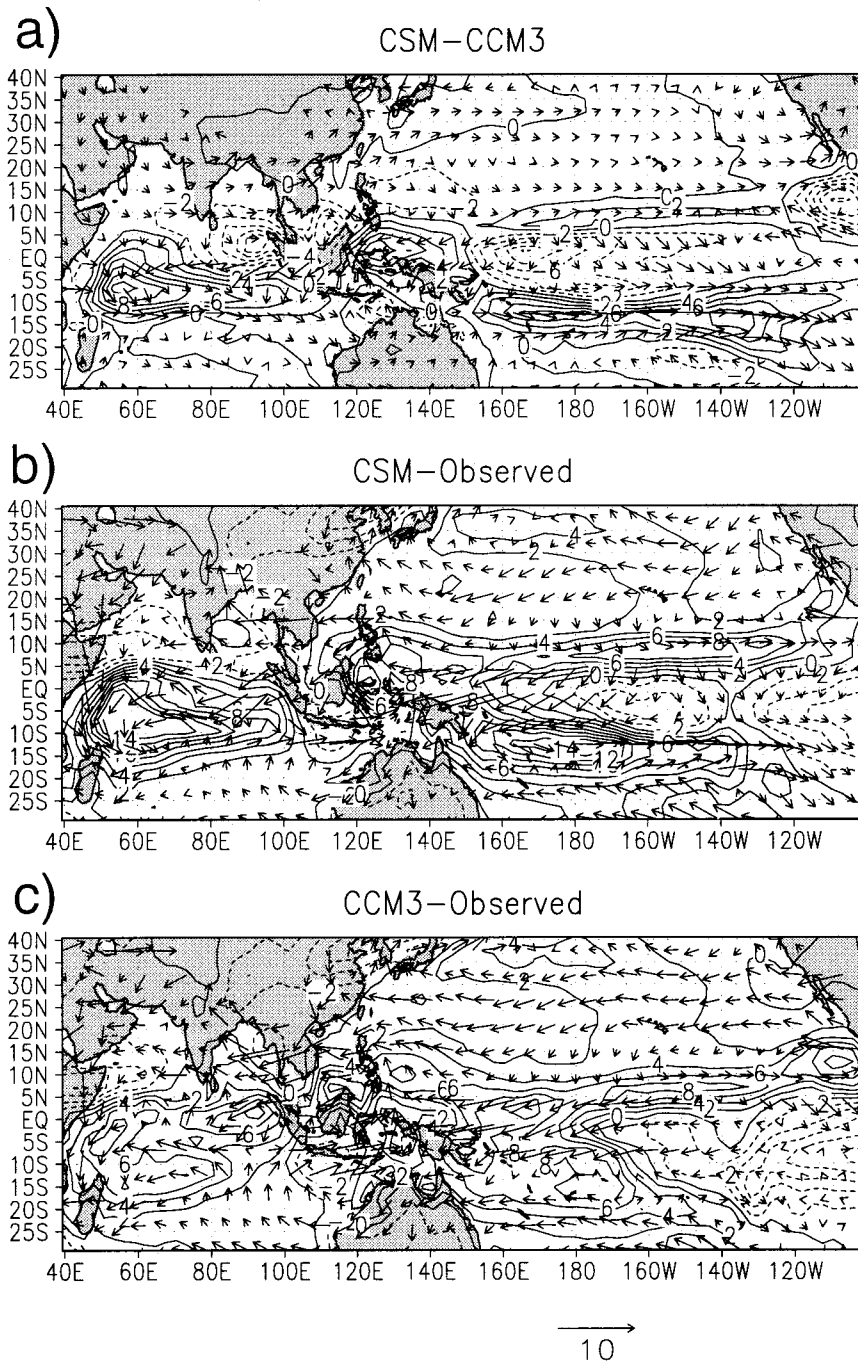b) CSM-Observed

c) CCM3-Observed

10

FIG. 4. (a) Precipitation and 850-mb wind vector differences, DJF, 45-yr averages for CSM minus CCM3; (b) same as (a) except for CSM−observations [NCAR–NCEP reanalyses for winds, Xie and Arkin (1996) for precipitation]; (c) same as (b) except for CCM3− observations; (d) DJF sea surface temperature differences, CSM−observations from the NCAR–NCEP reanalysis period from 1979 to 1995; (e) DJF latent heat flux differences, 45-yr averages, CSM–CCM3.

DJF
Long–term Average

d)

Sea Surface Temperature
CSM–Observed

e)
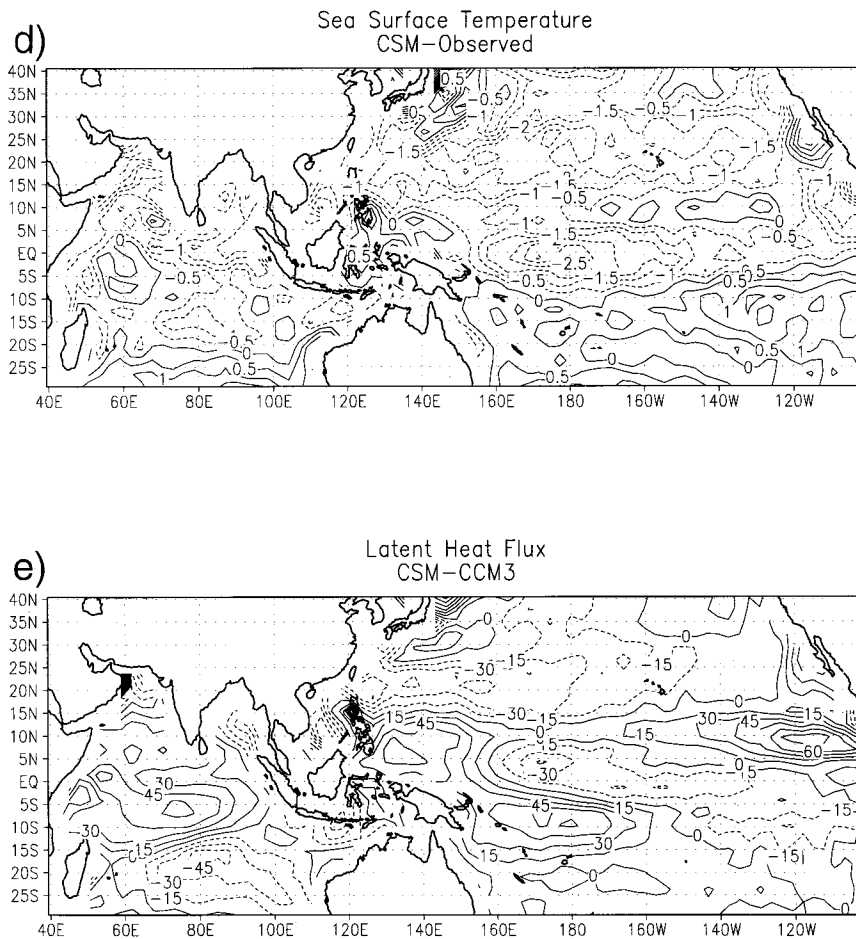
Latent Heat Flux
CSM–CCM3

FIG. 4. (*Continued*)

cipitation maxima, noted above to be about 6–9 mm day^{-1}, can be partly accounted for by the latent heat flux anomalies in those same regions of around 30–60 W m^{-2}. These would produce evaporation anomalies of about 1–2 mm day^{-1} locally. The remainder of the anomalous precipitation produced in CSM compared to the CCM3 is provided by low-level moisture flux convergence (not shown), as evidenced by the convergent vector wind anomalies near the precipitation anomaly centers in Fig. 2a. In the SPCZ region this is associated with an anomalous SST gradient as evidenced by larger positive SST errors east of 150°W noted previously in Fig. 2d. In particular, the large latent heat flux differences south of India in Fig. 2e of up to about 60 W m^{-2} are related to westerly low-level wind anomalies of about 5–10 m s^{-1} in Fig. 2a, with the strong winds better able to remove moisture from the surface. These low-level wind anomalies are associated with the precipitation anomaly near the Phil-

ippines mentioned above. Thus, to a first order in the tropical Indian and Pacific regions of the CSM, the SST errors in the coupled model are linked to the precipitation errors via changes in latent heat flux, evaporation, low-level winds, and low-level moisture flux convergence (see further discussion of these linkages in Meehl 1997b).

For the December–February (DJF) season in Fig. 3, the CSM again qualitatively reproduces the general patterns of tropical precipitation in the Indian–Pacific region, with greatest rainfall in the equatorial Indian Ocean, Pacific ITCZ and SPCZ, and Indonesia–Australia region, the latter associated with the Australian monsoon (cf. Figs. 3c and 3a). However, a more zonally oriented SPCZ is again evident in the southwest Pacific in the CSM (cf. Figs. 3a and 3c) along with anomalously large precipitation in the Celebes Sea east of Borneo. There are also greater precipitation amounts in the western Indian Ocean (Fig. 3c) compared to both

the observations (Fig. 3a) and CCM3 (Fig. 3b). Both the CCM3 and CSM simulate a shift of the precipitation maximum in the Australian monsoon from northeast Australia in the observations to northwest Australia in the models. As in JJA in Figs. 1 and 2, the CCM3 simulates greater than observed magnitudes of regional precipitation, with 6–9 mm day^{-1} anomalies (Fig. 4c) in all the regional precipitation maxima noted above. Thus the CSM reflects these magnitude errors in the CCM3 in the coupled simulation (Fig. 4b) but intensifies them by about 6 mm day^{-1}, particularly in the western Indian Ocean, Celebes Sea, and SPCZ (Fig. 4a). Westerly 850-mb wind anomalies of about 5 m s^{-1} northwest of Australia in Figs. 4b and 4c illustrate the stronger than observed Australian monsoon low-level flow in the CCM3 and CSM associated with the precipitation excesses in northwest Australia in the models. Upper-level wind differences at 200 mb (not shown) are consistent with the low-level wind and precipitation differences in Fig. 4 in that there is increased upper-level outflow to the west of Australia in the CCM3 and CSM compared to the observations.

As in JJA, the precipitation anomalies in the CSM can be partly attributed to errors in the SST simulation and associated SST gradient and low-level wind errors, with positive SST anomalies in the CSM of greater than +0.5C in the ITCZ, SPCZ, Celebes Sea, and western Indian Ocean (Fig. 4d) that, along with low-level wind anomalies, contribute to latent heat flux anomalies of about 30–50 W m^{-2} in those regions (Fig. 4e). This translates to evaporation anomalies of about 1–2 mm day^{-1} locally or only up to about one-third of the precipitation anomalies. Thus, as was noted for JJA above, the remaining 4 mm day^{-1} or so is contributed by low-level moisture flux convergence. Though not shown here, it can be seen that there is a significant contribution from anomalous low-level wind convergence seen in the vector differences in Fig. 4a. As in JJA, the elevated SSTs and low-level wind errors contribute to greater latent heat flux, more evaporation, increased low-level moisture convergence, and greater precipitation in the regional precipitation maxima in those areas in the CSM.

Another measure of a coupled model's ability to simulate mean climate is the equatorial SST gradient across the Pacific. Figure 5 shows this measure for several global coupled models, all without flux adjustment, compared to observations of SSTs from the Coupled Ocean–Atmosphere Data Set (COADS) as shown by Mechoso et al. (1995). Note that all the global coupled models simulate SSTs cooler than observed by about 1°–2°C but all roughly reproduce the right SST gradient across the Pacific from about 155°E to near 110°W. All models have more problems in the far western and far eastern Pacific, but the CSM more faithfully reproduces the character of the SST gradients in those regions.
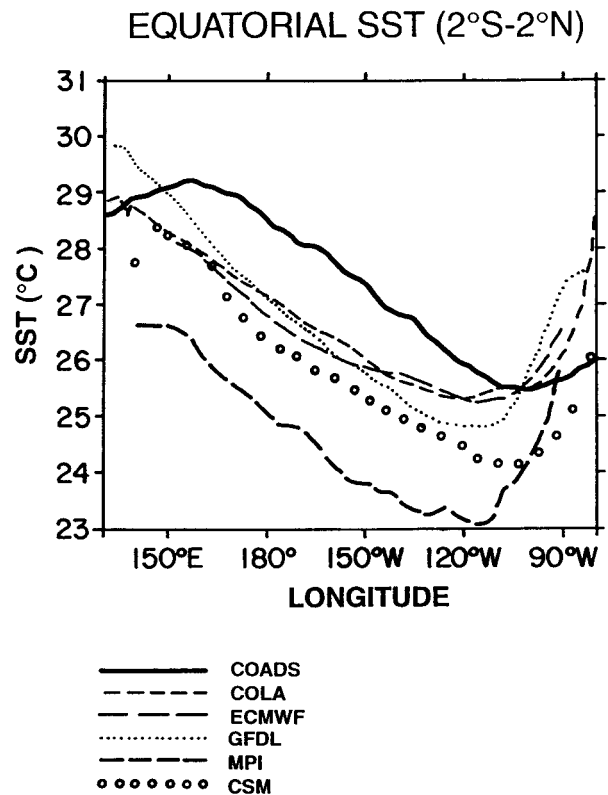

FIG. 5. SST gradient across the equatorial Pacific, averaged from 2°S to 2°N, for observations from COADS (solid line), three global coupled models (see key for model identification), and the CSM (open circles). All models do not use flux adjustment. Observed SST and coupled model results other than CSM taken from Mechoso et al. (1995). Note that this dataset of observed SSTs is somewhat different from that used in Figs. 2d and 4d.

3. The seasonal cycle in the tropical eastern Pacific

Mechoso et al. (1995) show the evolution of the seasonal cycle of monthly SSTs along the equator across the Pacific and note difficulties all the coupled models have in simulating this seasonal cycle. This is a demanding test of a coupled model due to the complicated coupled interactions taking place there (e.g., Neelin and Dijkstra 1995; Dijkstra and Neelin 1995). Figure 6a shows monthly anomalies (the annual mean is subtracted) from the SST observations of Shea et al. (1990). In the first half of the year, relatively warmer SSTs move progressively westward to be replaced by cooler SSTs that move westward in the second half of the year. Figure 6b shows a comparable plot from the CSM. There is more of a semiannual signal in the model, with the warmer SSTs in the first half of the year moving westward about 2 months later than in the observations. However, the reestablishment of the cooler water occurs at about the right time in the second half of the year but shows even stronger westward
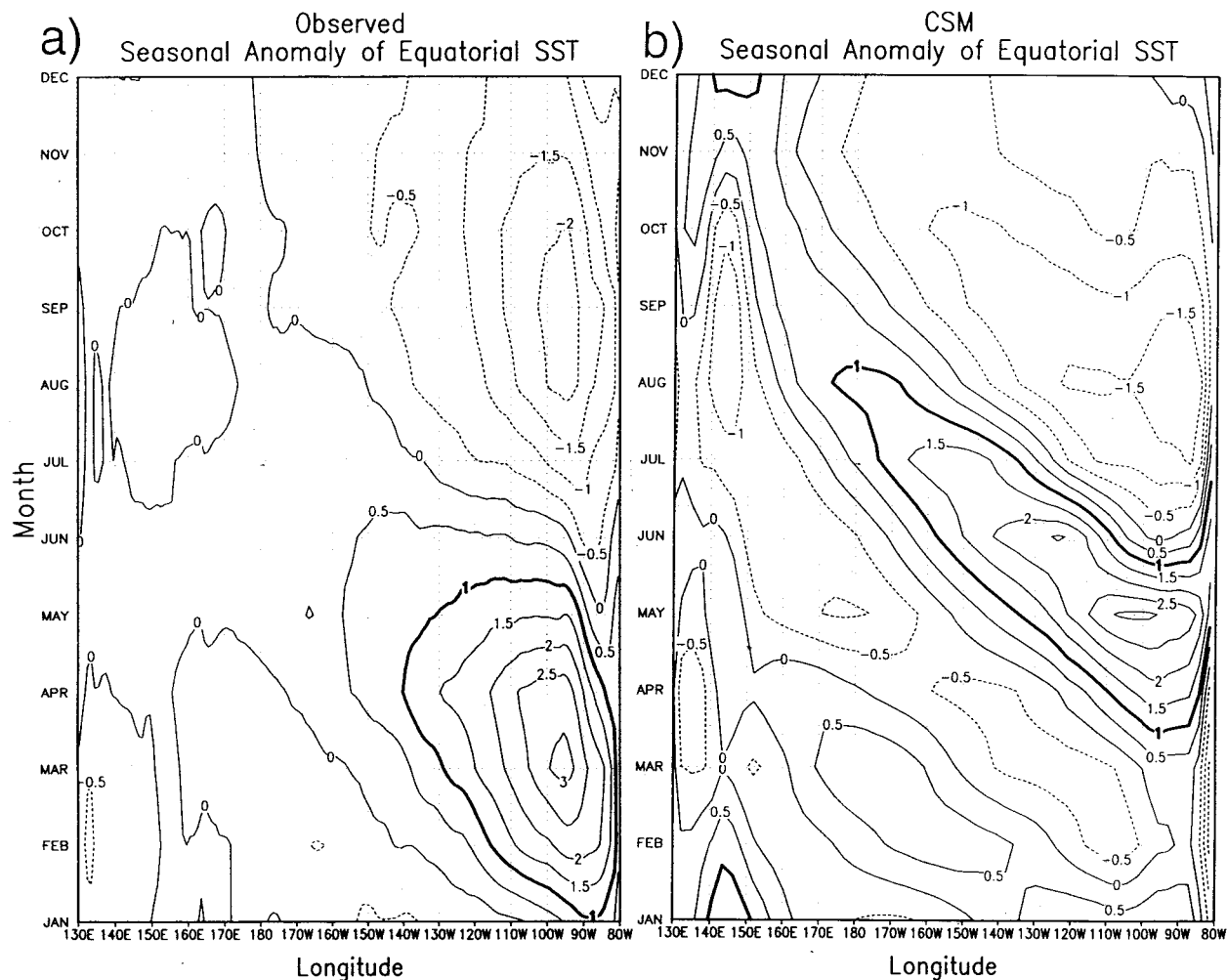
FIG. 6. Annual cycle of monthly mean SST (deviations from annual mean) across the Pacific averaged from 2°N to 2°S, +1°C contour darkened, for (a) observations of Shea et al. (1990) and (b) 45-yr averages from CSM.

propagation than the observations. This type of seasonal cycle, with the warm water progression delayed about 2 months at the beginning of the year, is characteristic of several of the global coupled models in the Mechoso et al. (1995) study and appears to be a systematic error in the current generation of coupled models. However, the CSM captures the amplitude of the seasonal cycle in the equatorial eastern Pacific reasonably well (with maximum positive values in the eastern Pacific of about 3°C and largest negative values of less than −1.5°C).

The seasonal cycle of precipitation in a sector of the eastern Pacific averaged from 150° to 100°W is shown in Fig. 7a for the observations of Xie and Arkin (1996) and in Fig. 7b for the CSM (long-term monthly means with the annual mean removed). The general characteristics of a stronger ITCZ north of the equator during the second half of the year and a double ITCZ during northern spring are reproduced by the CSM. However, the CSM tends to produce a southern ITCZ year round,

and particularly in northern spring when it is too strong, with the ITCZ maxima somewhat farther poleward than the observed (near 10°–12°S in northern spring, and around 10°–12°N for the northern ITCZ, compared to about 5°S and 8°–10°N, respectively, for the observations). Mechoso et al. (1995) show that the double ITCZ is a typical problem in global coupled models without flux adjustment. This could be partly related to the problems with inaccurate simulation of stratus clouds off the coast of South America or with details of the convective parameterization and the SST errors that result south of the equator in the eastern Pacific. Errors in the latitudinal position and breadth of the ITCZ are partly related to the relatively coarse atmospheric model resolution (Williamson et al. 1995), though the amplitude of the seasonal cycle is only marginally greater than the observed in the ITCZ maxima north of the equator (annual maximum values of about 12 mm day^{-1} for the observations and 14 mm day^{-1} for the CSM).

a)
Observed: XIE-ARKIN
Eastern Pacific Precipitation (mm/day)
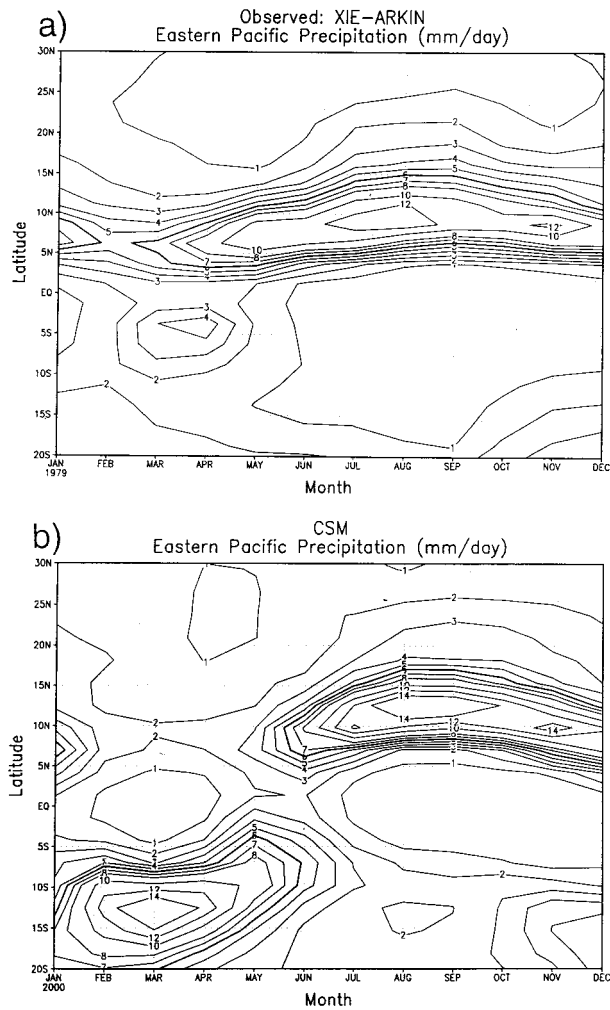

b)
CSM
Eastern Pacific Precipitation (mm/day)

FIG. 7. (a) Annual cycle of zonally averaged precipitation across the eastern Pacific (150°–100°W), 6 mm day^{-1} contour darkened; (b) same as (a) except for 45-yr averages from CSM.

4. Interannual variability

Time series of smoothed monthly mean area-averaged SST anomalies from the NINO3 region in the equatorial Pacific (150°–90°W, 5°N–5°S) for the 45-yr period under consideration from the CSM is superimposed on a recent 45-yr period from the observations (1950–94) and is shown in Fig. 8a. The CSM is producing roughly 55%–60% the amplitude of the observations for this period. Standard deviations for the time series in Fig. 8a for the observations are 0.73°C (0.86°C for the unsmoothed time series) and 0.39°C (0.49°C) for the CSM.

A time series for the same periods of CSM and observations as in Fig. 8a is shown for the Southern Oscillation index [SOI, a measure of the sea level pressure (SLP) difference for Tahiti minus Darwin] in Fig. 8b. Again the CSM has about 60% of the amplitude of the observations. The standard deviation of the smoothed time series of SOI in Fig. 8b for the observations is

a) .NINO-3 SST ANOMALIES: Observed (solid) and CSM (dashed)

b) .SOI (Tahiti-Darwin): Observed (solid) and CSM (dashed)

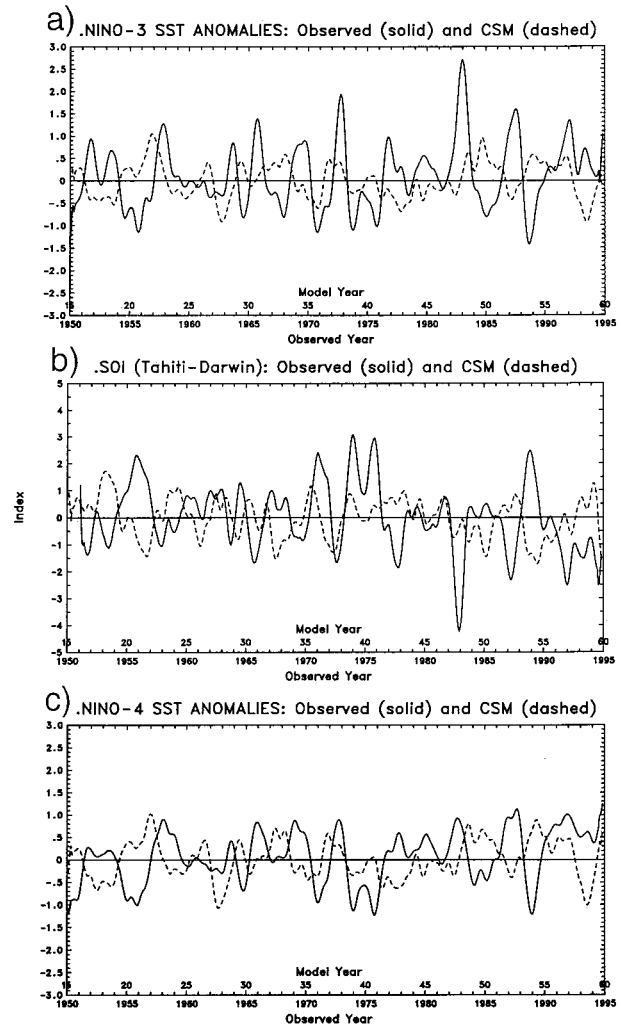c) .NINO-4 SST ANOMALIES: Observed (solid) and CSM (dashed)

FIG. 8. Smoothed monthly mean time series (11-point smoother) from the 45-yr CSM integration (dashed) and for observations for the 45-yr period 1950–94, for (a) area-averaged NINO3 (5°N–5°S, 90°–150°W) SST anomalies; (b) Southern Oscillation index; (c) area-averaged NINO4 (5°N–5°S, 160°E–150°W) SST anomalies. Model values superimposed on observations do not imply predictability but simply illustrate relative amplitude of variability of the CSM compared to observations.

1.23 mb (1.65 mb for the unsmoothed time series) and 0.72 mb (1.30 mb) for the CSM.

Comparable time series for the NINO4 area-averaged SST anomalies (5°N–5°S, 160°E–150°W) in the central equatorial Pacific in Fig. 8c shows the CSM and observations closer in amplitude, with the observations having a standard deviation for the smoothed time series of 0.58°C (0.64°C unsmoothed), and 0.43°C (0.55°C) for the CSM. As will be seen later, this is symptomatic of greater interannual variability of SSTs in the CSM in the western equatorial Pacific than the east compared to observations. Current global coupled models typically show amplitudes in these measures less than observed (Meehl 1995) with the models sim-

ulating either somewhat less or similar amplitude of NINO3 SST anomalies compared to the CSM. For example, the Hadley Centre coupled model in the United Kingdom (Tett 1995) shows amplitudes of NINO3 SST anomalies about half the observed, while the Meteorological Research Institute model in Japan (Yukimoto et al. 1996) is roughly comparable to the CSM. A recent version of a global coupled model at the Max-Planck Institute in Germany (Roeckner et al. 1996) has comparable or slighter greater amplitude tropical Pacific SST variability compared to the CSM.

A more challenging test of a coupled model is to reproduce the spatial patterns of interannual variability. Figure 9 shows the correlation of the SOI with surface temperatures for observations, the CCM3, and the CSM. The observations and models all show negative correlations of up to -0.8 in the eastern tropical Pacific and near -0.4 in the western Indian Ocean (negative SOI, as in an ENSO event, associated with positive SST anomalies in those areas), and positive correlations of $+0.4$ to $+0.6$ over the western tropical Pacific and near 30°N and 30°S in the Pacific (negative SOI associated with negative SST anomalies in those areas). All of these correlations are significant at the 5% level. As could be expected from the results in Fig. 8, the amplitude of the correlations is about 20% less in the CSM due to the lower-amplitude SOI and SST variability.

Note in the observations in Fig. 9a the association of negative correlations over parts of India, central Asia, and east Asia with negative correlations over the eastern tropical Pacific. As noted previously (Kiladis and van Loon 1988; Meehl 1995, 1997a) a year with negative SOI indicative of lower SLP over the eastern Pacific and higher SLP over the Indian sector is often associated with positive SST anomalies in the eastern Pacific and positive land surface temperature anomalies over much of south Asia. This is indicative of the linkages between the Indian monsoon, the tropical Pacific, and the tropospheric biennial oscillation (TBO), whereby the following year has the opposite pattern with negative SST anomalies in the eastern tropical Pacific and negative land surface temperature anomalies over south Asia. The role of the land surface temperature anomalies is to set up regional-scale land–sea (or meridional) temperature gradients that influence the subsequent monsoon. Thus, as outlined by Meehl (1995, 1997a), the positive SST anomalies in the eastern Pacific are associated with a weak monsoon, less rainfall, less ground wetness, and relatively warm land temperatures. These warm land temperatures set up increased land–sea temperature contrast for a strong monsoon the following year and the opposite set of anomalies. Negative correlations over parts of south Asia in Fig. 9a are roughly -0.4 and significant at the 5% level. In the CCM3 in Fig. 9b, the correlations over this region drop to around -0.2 to -0.3, and in the CSM in Fig. 9c they drop again to -0.2 or less with

more areas of positive correlations. Thus, the CSM appears to reproduce some of the linkages between the south Asian monsoon and tropical Pacific SSTs (this will be explored in greater detail below) but not all of the land surface connections to interannual variability in the Pacific SSTs. The indication is that the CSM will be able to simulate the TBO but with lower amplitude compared to observations. This aspect of the CSM simulation will be discussed in Fig. 14 and is under further investigation.

Additionally, the CSM has a general tendency to maintain positive correlations in the South China Sea and eastern Indian Ocean where the observations show negative correlations. Positive correlations in the tropical Atlantic in the observations and CCM3 are not reproduced in the CSM, though the negative correlations across tropical South America are simulated in the CSM. The area of negative correlations in the tropical eastern Pacific is reduced in latitudinal extent in the CSM compared to the observations and CCM3, consistent with the SST errors shown in Figs. 2 and 4.

Another measure of spatial relationships of interannual variability in the observations and CSM is given in Fig. 10, which is the correlation of NINO3 SST anomalies with global SLP. As in Fig. 9, the large-scale aspects of the observed (Fig. 10a) east–west atmospheric circulation and SSTs in the tropical Pacific–Indian Ocean region are reproduced in the CCM3 (Fig. 10b) and CSM (Fig. 10c). Observations and models all show negative correlations of around -0.8 in the tropical eastern Pacific (low pressure overlies warm water) and correlations of $+0.6$ to $+0.8$ in the western Pacific and Indian Oceans, all significant at the 5% level. There are also negative correlations in all three panels of Fig. 10 of around -0.2 to -0.4 in the Pacific Ocean near 50°N and 50°S, and positive correlations in the northwest and southwest Pacific of about $+0.4$ to $+0.6$. Links to the Asian and Australian monsoons are also evident in Fig. 10 for observations and the model simulations with positive correlations of around $+0.6$ to $+0.8$ lying over these regions. This reflects the relationship between the Southern Oscillation (out of phase sea level pressure anomalies between the tropical Indian–west Pacific Ocean and eastern tropical Pacific in association with NINO3 SSTs that are high when SLP is low over the eastern Pacific) and the Asian–Australian monsoons (relatively high SLP associated with suppressed precipitation and weak monsoons).

However, to better understand the relationship between the tropical Pacific SSTs and the Asian–Australian monsoons in the model simulations, it is important to note the longitudinal position of the zero line separating negative correlations over the equatorial Pacific and positive correlations over the western Pacific–Indian sector. In the observations (Fig. 10a) and the CCM3 (Fig. 10b), the zero line lies near the date line. In the CSM it is shifted westward to about 150°E. This is associated with a corresponding westward shift of the area covered by the $+0.8$ contour that, in the observations, extends from India
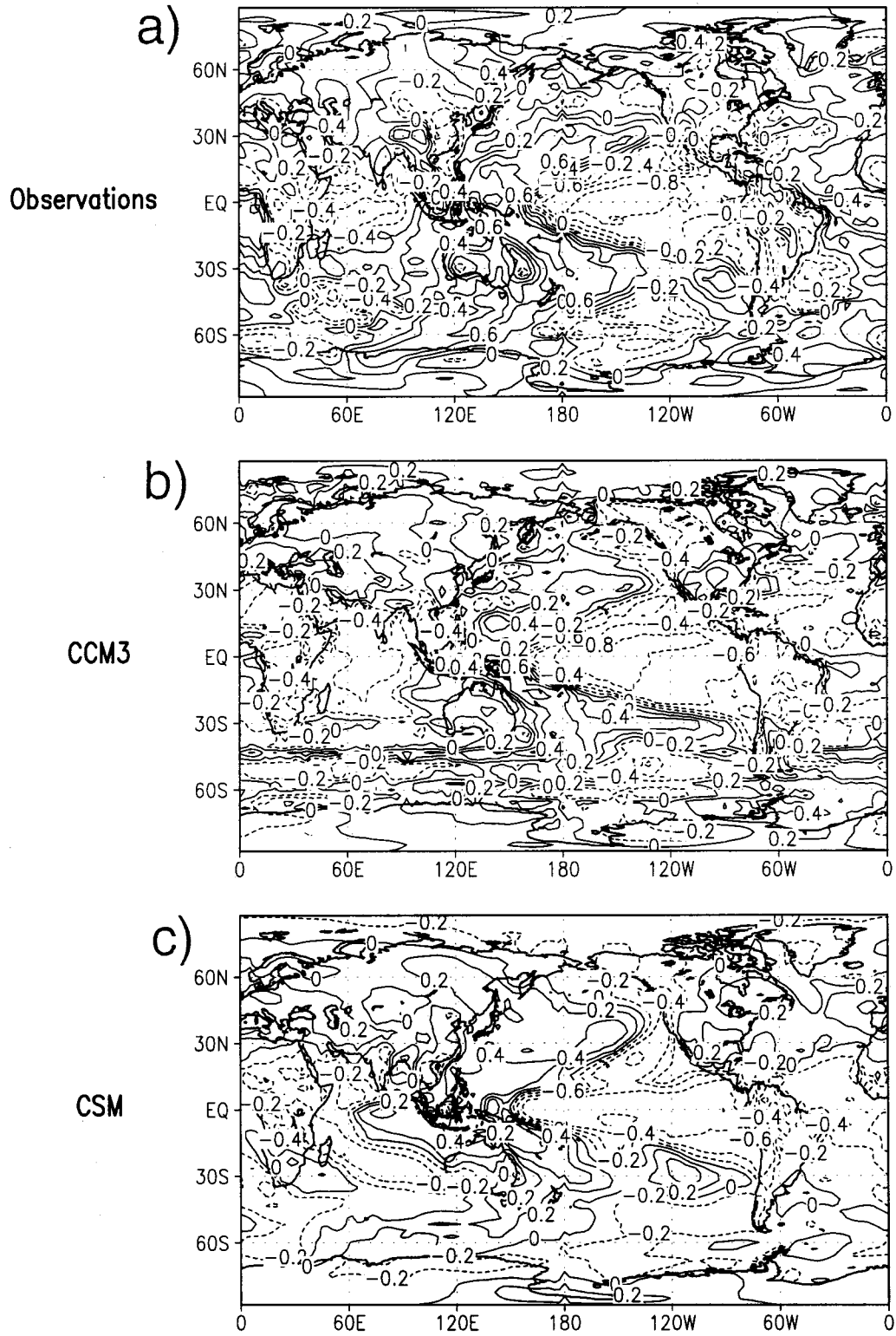
FIG. 9. Correlation of annual mean SOI with global distribution of annual mean surface temperature for (a) observations (NCAR–NCEP reanalyses) for the period 1979–95; (b) CCM3 for the period 1950–94; (c) 45-yr period from CSM.
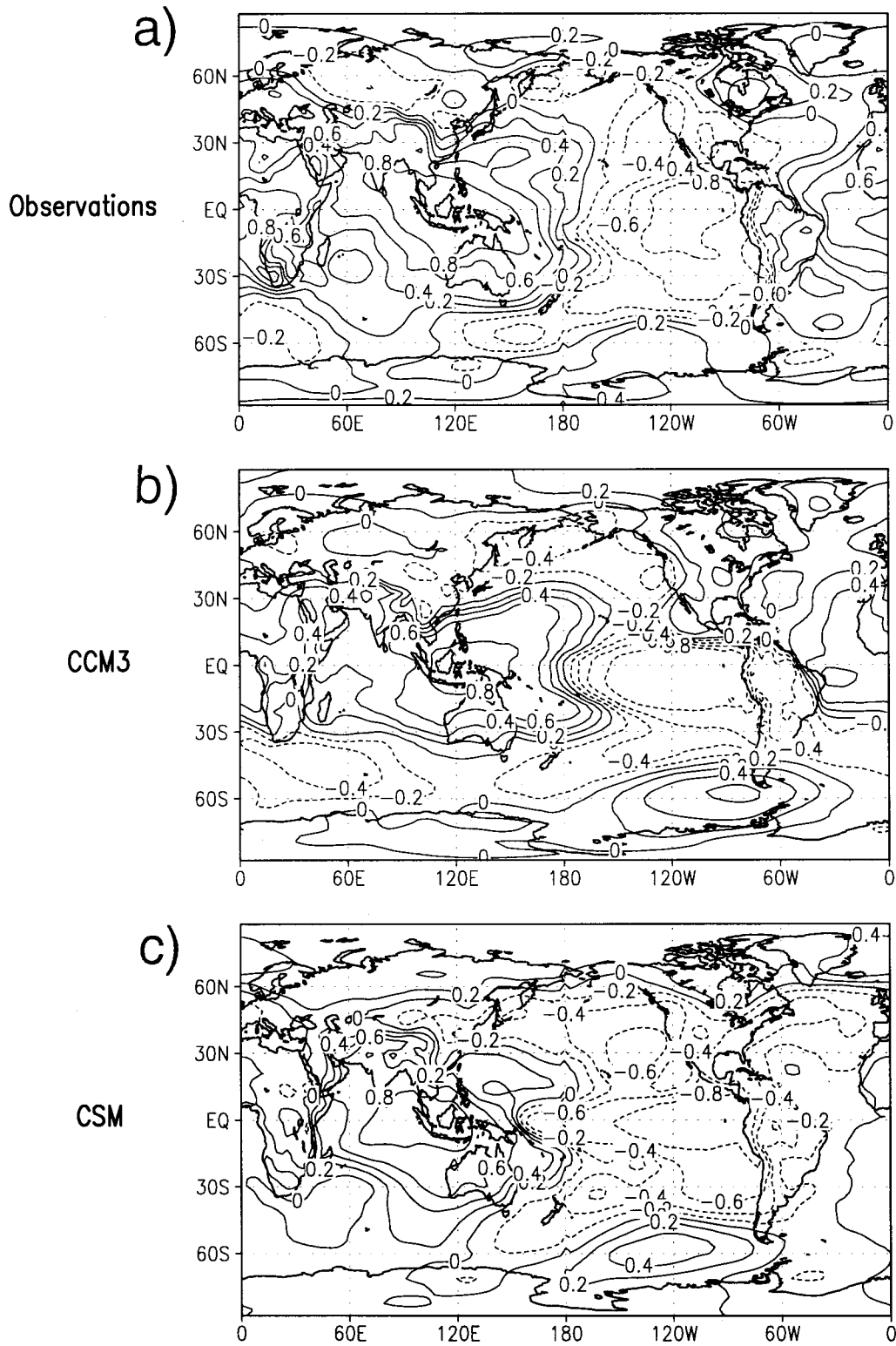
FIG. 10. Correlation of annual mean NINO3 SST anomalies with global distribution of sea level pressure for (a) observations (NCAR–NCEP reanalyses) for the period 1979–95; (b) CCM3 for the period 1950–94; (c) 45-yr period from CSM.
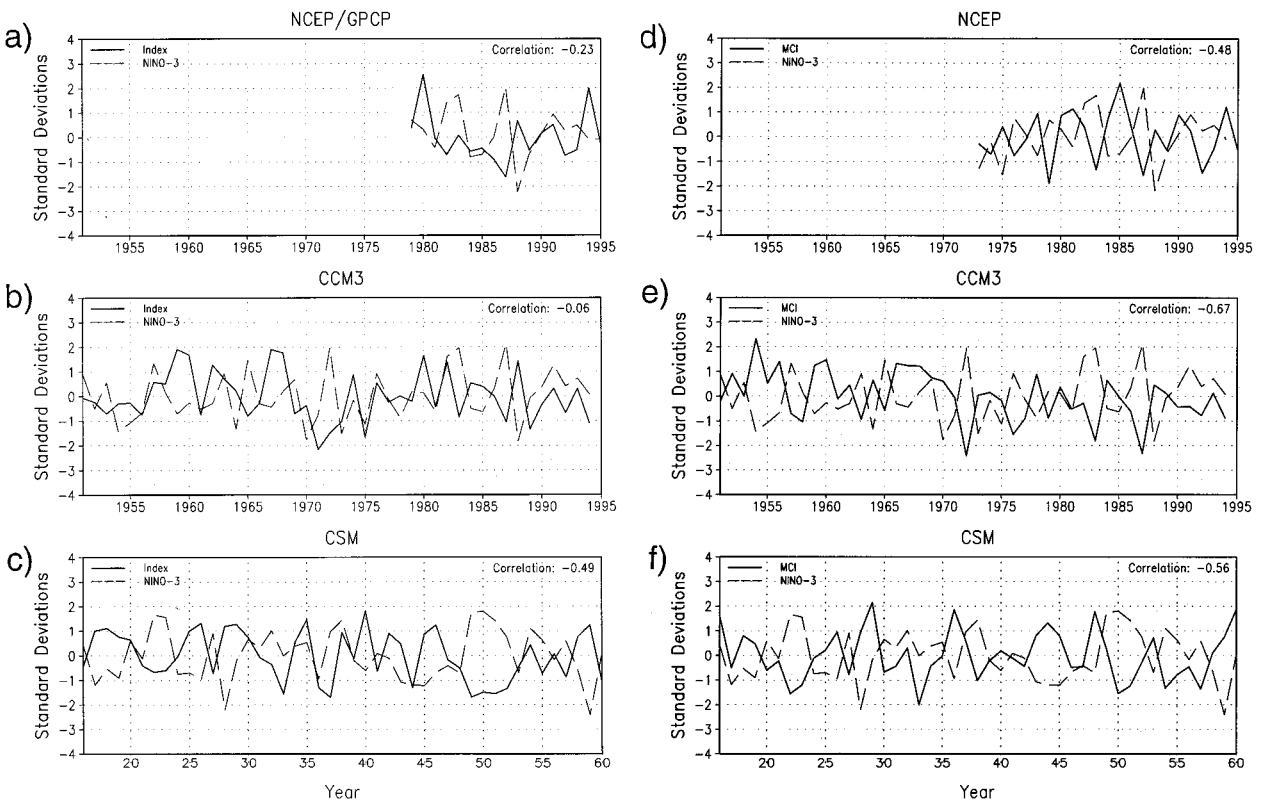
FIG. 11. Normalized time series of all-India rainfall index (land points only in the area 5°–30°N, 70°–90°E, JJA), solid line, and NINO3 SSTs (JJA), dashed line for (a) NINO3 SST anomalies from the NCAR–NCEP reanalyses, 1979–95, and rainfall from Xie and Arkin (1996); (b) the CCM3 integration from 1950 to 1994; (c) the 45-yr period from the CSM; (d) same as (a) except using the monsoon circulation index (MCI; u wind anomalies at 850 mb − 200 mb over the area 0°–20°N, 40°–110°E); (e) same as (b) except using the MCI; (f) same as (c) except using the MCI. Correlation coefficients between the two time series in each frame are given in the upper right-hand corners.

eastward to near 160°E. In CCM3 that area shrinks to a region from around 105°E to 150°E, while in CSM the area again extends to India in the west but only to near 130°E at the eastern limit. Thus the implication is that the CCM3 will have less strong associations between the Indian monsoon and NINO3 SSTs, but it will have strong links between the Australian monsoon and NINO3 SSTs. Meanwhile the CSM will be opposite to the CCM3 with stronger links between NINO3 SSTs and the Indian monsoon but weaker connections to the Australian monsoon. This aspect of the large-scale east–west circulations linking the Asian–Australian monsoons and equatorial Pacific SSTs will be discussed further below.

5. Connections between the Pacific and the Asian–Australian Monsoon

Normalized time series of two different Asian summer monsoon indices are plotted with normalized NINO3 SST anomalies in Fig. 11 for models and observations. The Indian monsoon rainfall index (IMRI) is precipitation averaged over India (land points in the area 5°–30°N, 70°–90°E) for JJA and is comparable to observed long-term indices for the Indian monsoon such as the one of Parthasarathy et al. (1991). Standard

deviation of the IMRI for the CSM is 0.70 mm day⁻¹. An IMRI time series calculated from the Xie and Arkin observed precipitation dataset (1979–95) for the same grid points over India as those from the model shows a standard deviation 13% greater than the CSM with a value of 0.79 mm day⁻¹. This is consistent with the general model characteristic of less than observed interannual variability amplitude, though such an index from the model should able to represent the observed interannual linkages between monsoon strength and tropical Pacific SSTs (e.g., Shukla 1987; Meehl 1994). The monsoon circulation index (MCI) follows the definition of Webster and Yang (1992) and is the difference of anomalous 850-mb wind minus anomalous 200-mb u wind over the area 0°–20°N, 40°–110°E. As discussed by Webster and Yang (1992), the MCI is a regional-scale dynamical index thought to be more indicative of the strength of the monsoon over the entire south Asian region. Both the IMRI and MCI show an inverse relationship with NINO3 SST in observations and models such that strong monsoons are generally associated with negative SST anomalies in the eastern Pacific.

Correlations in Fig. 11 are given in the upper right-hand corners of the panels and are −0.23 for the ob-

served IMRI (calculated from the Xie and Arkin precipitation dataset for the years 1979–95) and NINO3 SST, −0.06 for the CCM3, and −0.49 for the CSM. The correlation for the observations is −0.56 if the updated Parthasarathy et al. Indian monsoon rainfall index is correlated with NINO3 SSTs for the period 1950–94, with a lower correlation of −0.37 if the period 1979–94 is used. This latter number is for the comparable period that produced a correlation of −0.23 using the area-averaged gridded precipitation from Xie and Arkin. The changes in magnitudes of the observed correlations for different time periods are indicative of secular fluctuations in the strength of the observed east–west connections between NINO3 SSTs and Indian monsoon rainfall. Yet the general relationship of relatively cold NINO3 SSTs with strong monsoons seems to hold for all periods.

Even though there are errors in the simulation of details of regional rainfall over India in the CSM (Fig. 1), the large-scale east–west linkages are still functioning in the model as has been documented for other coupled models (e.g., Meehl 1994). Also note that the relationships are somewhat different for the MCI in Figs. 11d–f. The observed correlation between MCI (calculated from the NCAR–NCEP reanalysis data for the period 1973–95) and NINO3 SSTs is −0.48, and it is −0.67 for CCM3 and −0.56 for the CSM.

The greatest change in correlations is for the CCM3, where there is almost no relationship between the IMRI and NINO3 SSTs but a significant (at the 5% level) negative correlation for the MCI and NINO3 SSTs. In comparing the models from the Atmospheric Model Intercomparison Project (AMIP), Sperber and Palmer (1996) documented a similar phenomenon for the ensemble of atmospheric models. The models were more successful in reproducing the dynamical index (MCI) but had less skill in simulating the rainfall index for India. Since the CCM3 at T42 resolution is in the same class as many of the models in AMIP, the suggestion is that rainfall distributions are more difficult to simulate over a finite area such as India compared to a large-scale circulation index indicative of dynamical processes occurring over a large area of south Asia. However, the CSM, using the same CCM3 but coupled to the dynamical ocean, is more successful in simulating the IMRI links to NINO3 SSTs compared to the CCM3 (correlations of −0.06 for the CCM3 compared to −0.49 for the CSM). The implication, which needs to be explored further, is that a model with internal dynamical consistency (the CSM being a coupled ocean–atmosphere model) may be better able to reproduce linkages between large-scale circulation and regional rainfall regimes. There are also factors at work relating the location of the centers of the large-scale east–west circulation in the observations and models. As discussed above in relation to Fig. 10, the region of largest correlations between sea level pressure and NINO3 SSTs contracts in CCM3 to fall only over the
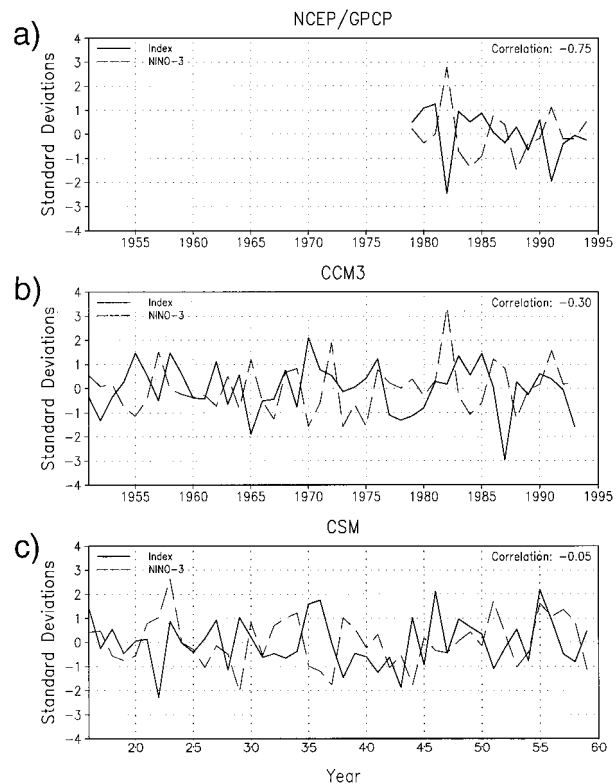

FIG. 12. Normalized time series of Australian monsoon rainfall index (all points in the area 15°S–0°, 110°–150°E, DJF), solid line, and NINO3 SSTs (DJF), dashed line for (a) NINO3 SST anomalies from the NCAR–NCEP reanalyses, 1979–95, and rainfall from Xie and Arkin (1996); (b) the CCM3 integration from 1950 to 1994; (c) the 45-yr period from the CSM. Correlation coefficients between the two time series in each frame are given in the upper right-hand corners.

Indonesian region, while in CSM the center of largest correlations shifts westward to lie partly over southern India. This shift is associated with a westward movement of the nodal line between positive and negative correlations in the tropical Pacific.

Similar time series for an Australian monsoon index of area-averaged rainfall for the DJF season over the area 15°S–0°, 110°–150°E (including most areas of maximum precipitation for that region during the Australian monsoon season in Fig. 3) and for NINO3 SSTs are shown in Fig. 12. The linkages between this monsoon regime show observed correlations of −0.75 (strong Australian monsoons being associated with negative SST anomalies in the NINO3 region), while the CCM3 has a correlation of −0.30 compared to the CSM with only a correlation of −0.05. The reduced negative correlation in the CSM is related to the stronger than observed cold tongue extending across the equatorial Pacific (Figs. 3 and 4). As noted above, this is associated with a westward shift of the area of maximum correlations between NINO3 SSTs and SLP in the western Pacific comparing Figs. 10a,b to Fig. 10c. Thus, the Australian monsoon in the CSM is closer to
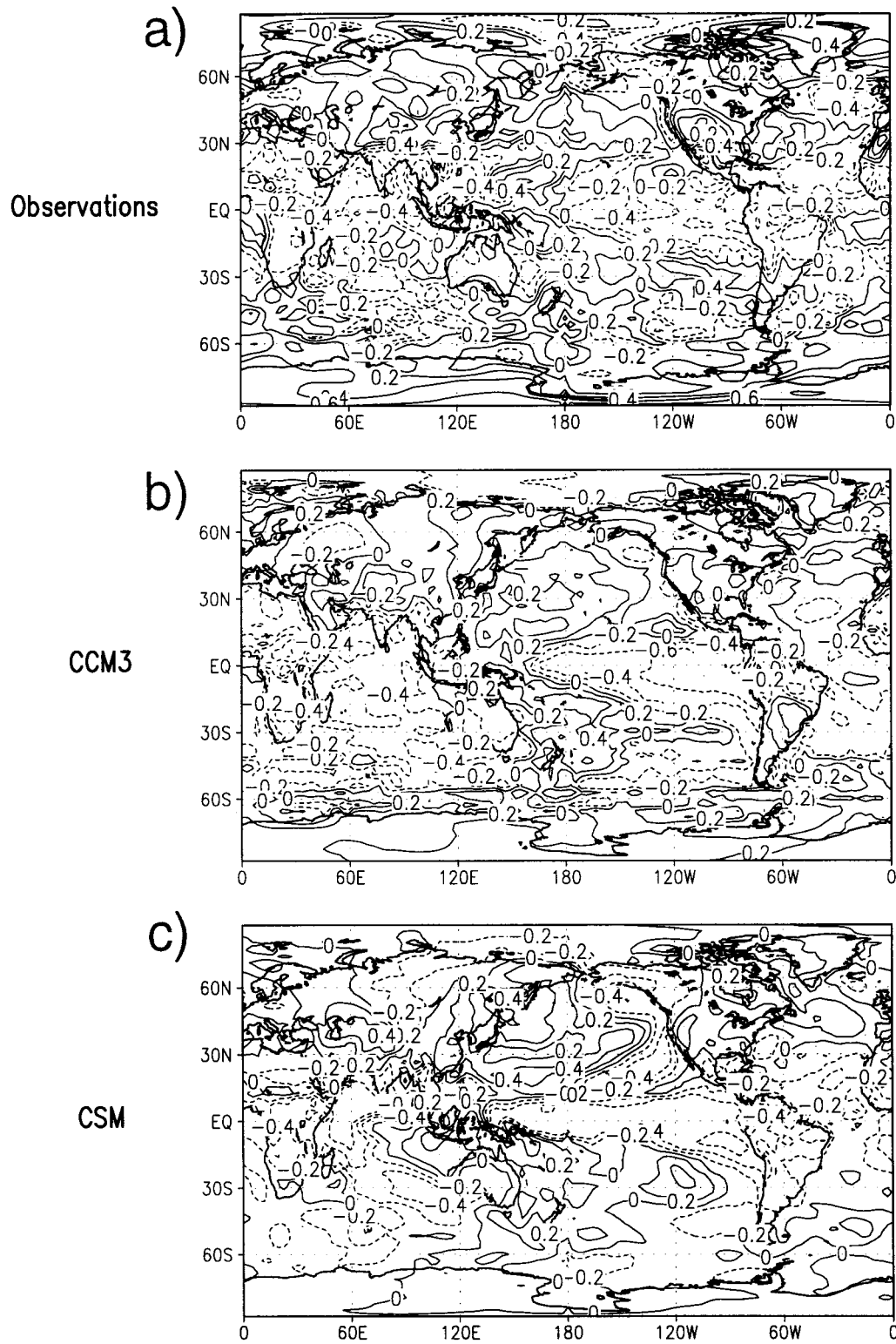
FIG. 13. Correlation of Indian monsoon circulation index (MCI, u wind anomalies at 850 mb $-$ 200 mb over the area 0°–20°N, 40°–110°E) and global distribution of surface temperature (JJA) for (a) observations from NCAR–NCEP reanalyses (1979–95), (b) CCM3 for the period 1950–94; (c) 45-yr period from CSM; (d) same as (a) except for the Australian monsoon rainfall index (all points in the area 15°S–0°, 110°–150°E, DJF); (e) same as (b) except for rainfall index from CCM3; (f) same as (c) except for rainfall index from CSM.

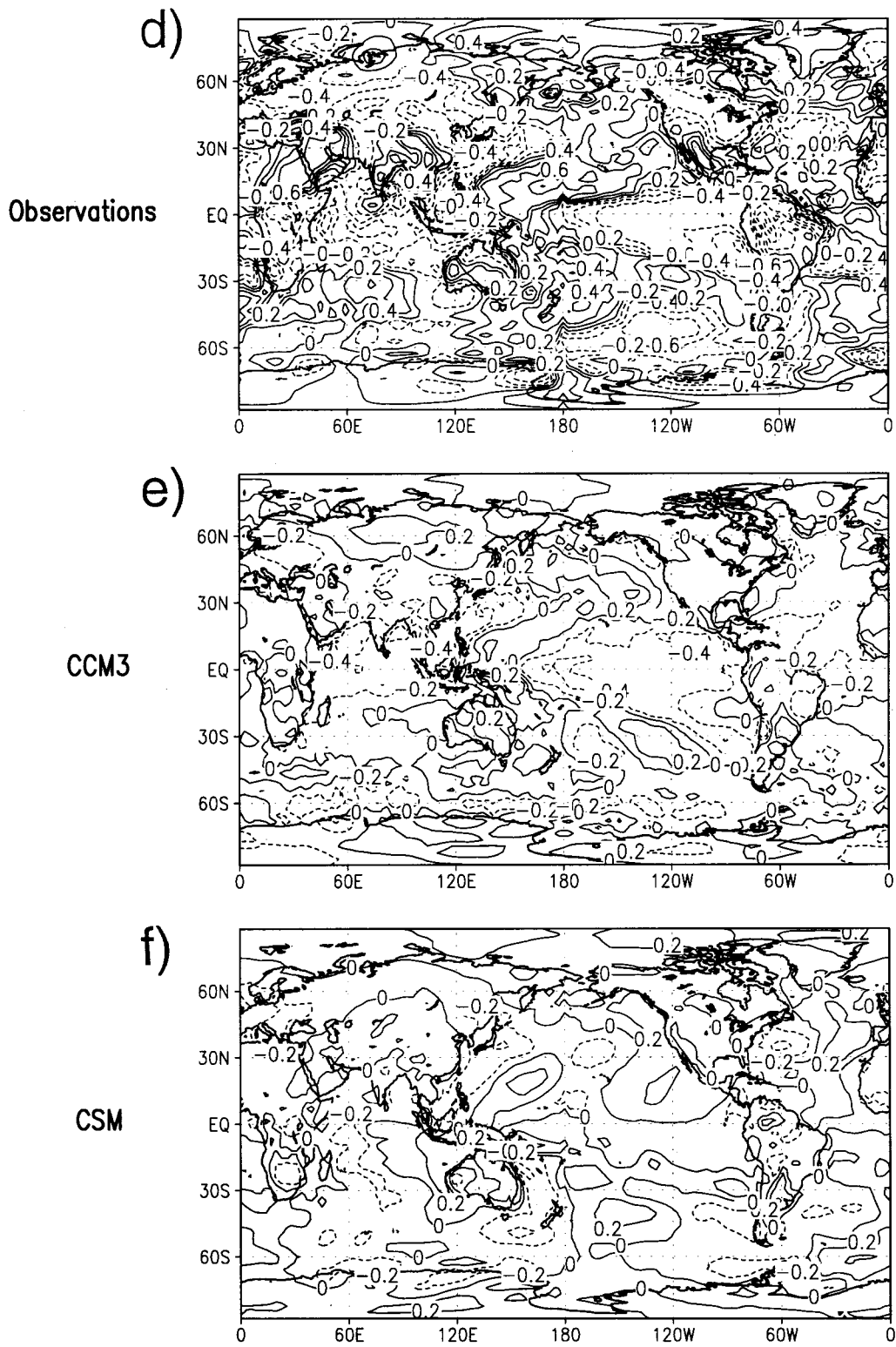d)

Observations

e)

CCM3

f)

CSM

Fig. 13. (*Continued*)

the nodal line of the Walker circulation, while in the observations the Australian monsoon lies more in the rising branch with opposite sign anomalies over the tropical Pacific.

The spatial patterns associated with the relationships between the Asian–Australian monsoons and large-scale atmospheric circulation are shown as the correlation between the MCI and global surface temperatures (Figs. 13a–c) and the Australian monsoon index and global surface temperatures (Figs. 13d–f). As suggested by the time series correlations between the MCI and NINO3 SSTs, there are negative correlations exceeding −0.4 for the observations, CCM3, and CSM over the tropical Pacific. For observations and both model simulations, there are also negative correlations over India of around −0.3 to −0.4, indicating that strong monsoons are associated with cold land surface temperatures. The observations, CCM3, and CSM show positive correlations over most areas of the northwest and southwest Pacific, similar to the pattern for the SOI and NINO3 SST correlations in Fig. 9.

Correlations calculated between the Australian monsoon rainfall index and global surface temperatures (Figs. 13d–f) are also consistent with the time series results in Fig. 11 in that observations and both models have negative correlations over most of the tropical Pacific with values exceeding −0.4 in the observations and CCM3, and with smaller-amplitude negative correlations of around −0.1 to −0.2 for the CSM. All three also show positive correlations over many areas of the northwest and southwest Pacific, with largest positive values (greater than +0.4) in the observations and CCM3 over the far western Pacific and Indonesia.

The timescales of monsoon variability for the CSM are shown in Figs. 14a,b, which are plots of the spectra of the IMRI and MCI. There are peaks in the spectra for both indices roughly in the timescales of the TBO (around 2.3–2.6 yr) and ENSO (around 5 yr), though for this 45-yr time series only the ENSO peak in the MCI is significant at the 5% level. Spectral peaks in the decadal, ENSO, and TBO timescales are similar to an observed monsoon index (see Meehl 1997a), and are also comparable to spectral peaks in observed large-scale precipitation patterns over the India–Pacific region (Lau and Sheu 1988). The TBO and ENSO are probably linked in various ways (e.g., Meehl 1987; Ropelewski et al. 1992), so the model results are encouraging in that they suggest that the CSM is capable of simulating at least some of these coupled processes for these timescales. Most of the spectral peaks, though physically notable, do not exceed the 95% significance level consistent with the less than observed amplitude of variability noted earlier (e.g., Fig. 8).

Meanwhile, spectra for the time series of NINO3 SSTs from the CSM (Fig. 14c) also show peaks in the TBO, ENSO, and decadal frequencies similar to the monsoon indices in Figs. 14a,b (and observed SST in the eastern Pacific; e.g., Rasmusson and Carpenter

1982) as could be expected from the linkages shown between the Asian monsoon and eastern Pacific SSTs above. The decadal and TBO peaks for the NINO3 SSTs are not as pronounced as those for the monsoon index in Fig. 14a, while one of the NINO3 ENSO peaks with a period of about 4 yr in Fig. 14b is significant for this time series at the 95% level. Cospectra (not shown) show large coherence between the two monsoon indices and the NINO3 SST index on the decadal, ENSO, and TBO timescales. However, due to the relatively weaker linkage between the Australian monsoon and NINO3 SSTs discussed in Figs. 10 and 12 above, the spectra for the Australian monsoon index in Fig. 14c has spectral peaks at somewhat different frequencies compared to the NINO3 SST spectra in Fig. 14d, and thus there is proportionately less coherence between the two (not shown).

6. ENSO-like features in the CSM

As noted earlier, the CSM simulates interannual variability in the eastern equatorial Pacific SSTs with a reduced amplitude compared to observations (see Fig. 8). Here we examine some of the time–space characteristics of the associated ENSO-like variability in the CSM. Figure 15a shows observations (1982–90; S. Tett 1997, personal communication) of lag correlations between a time series of area-averaged SST near the NINO3 region (in this case 5°N–5°S, 90°–105°W; data from the Global Sea-Ice and Sea Surface Temperature Data Set (GISST)) and vertically averaged temperature as an indicator of heat content in the top 360 m (5°N–5°S across the Pacific; data from NCEP analysis). The observations show eastward propagation of upper oceanic heat content anomalies with a phase speed of about 0.2 m s⁻¹. Positive heat content anomalies form in the western Pacific 18 months prior to the largest positive warm SST anomalies in the eastern equatorial Pacific (lag correlations of greater than +0.5) and propagate eastward. At lag 0, largest positive heat content anomalies in the eastern equatorial Pacific correspond to warmest SSTs there (correlations of greater than +0.8). The positive heat content anomalies are then followed by negative heat content anomalies that also propagate from the western to eastern Pacific. Largest negative values appear in the western Pacific a couple months after lag 0 and move into the eastern Pacific over the next 18 months.

A similar calculation is performed for the CSM and is shown in Fig. 15b. Here, the time series of NINO3 SST from Fig. 8a is lag-correlated with vertically averaged temperature in the top 360 m averaged from 5°N to 5°S. There is a similar pattern to the observations, with eastward-propagating upper-ocean heat content anomalies with a phase speed of about 0.3 m s⁻¹, somewhat faster than the observed value of about 0.2 m s⁻¹ in Fig. 15a. There is good qualitative agreement between the CSM in Fig. 15b and the observations in Fig. 15a, with positive heat content anomalies forming in the
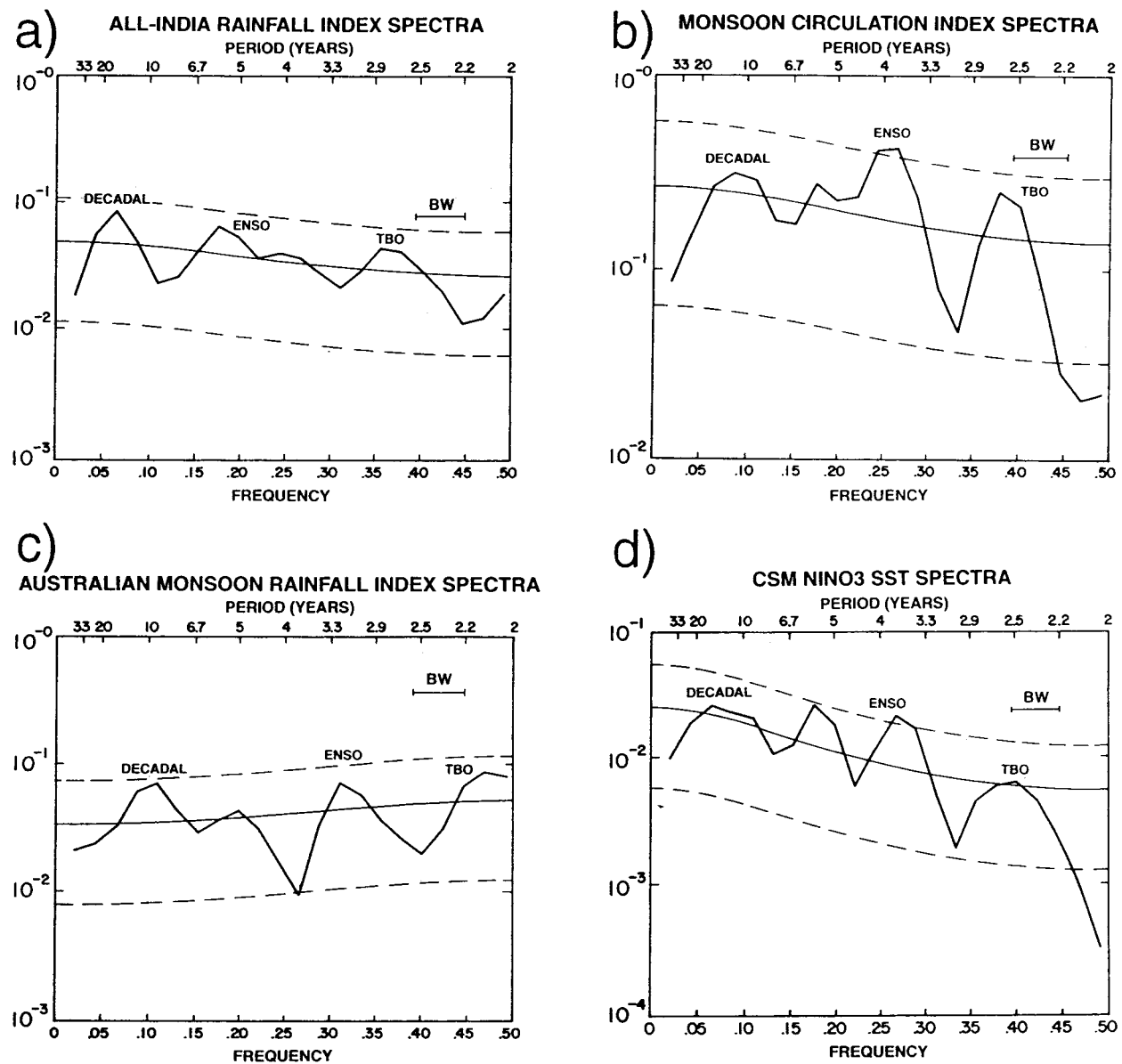
FIG. 14. (a) Spectra of JJA all-India monsoon rainfall index from 45-yr period of CSM. Red noise estimate is thin solid line, upper dashed line is 95% significance level. Band width is denoted "BW" in figure. Decadal, ENSO, and TBO peaks are noted. (b) Same as (a) except for the monsoon circulation index (MCI). (c) Same as (a) except for the Australian monsoon index for DJF. (d) Same as (a) except for annual mean NINO3 SSTs.

western Pacific at lag −18 months, moving eastward to correspond to largest positive NINO3 SST anomalies at lag 0 in the eastern Pacific, followed by negative heat content anomalies that form in the western Pacific and propagate to the eastern Pacific over the next 18 months. The values of the lag correlations are larger in the observations with greater stippled areas of lag correlations larger than 0.4 and maxima away from the NINO3 area of about 0.6–0.7 compared to 0.4–0.5 in the CSM. This is associated with the general reduction of interannual variability in the tropical Pacific in the CSM compared to the observations noted in Fig. 8. In spite of that

limitation, the pattern and phase speed of the heat content anomalies from the CSM compare more favorably to the observations than several other coupled models shown by S. Tett (1997, personal communication). In that study, similar plots from three other coupled models of varying configurations and resolutions show even faster eastward propagation of heat content anomalies than in either the observations or the CSM.

To examine the time evolution of El Niño- and La Niña-like events in the CSM, composites are formed for years in Fig. 8a where the smoothed NINO3 SST anomaly first exceeds +0.5°C (for El Niño-like events) or is
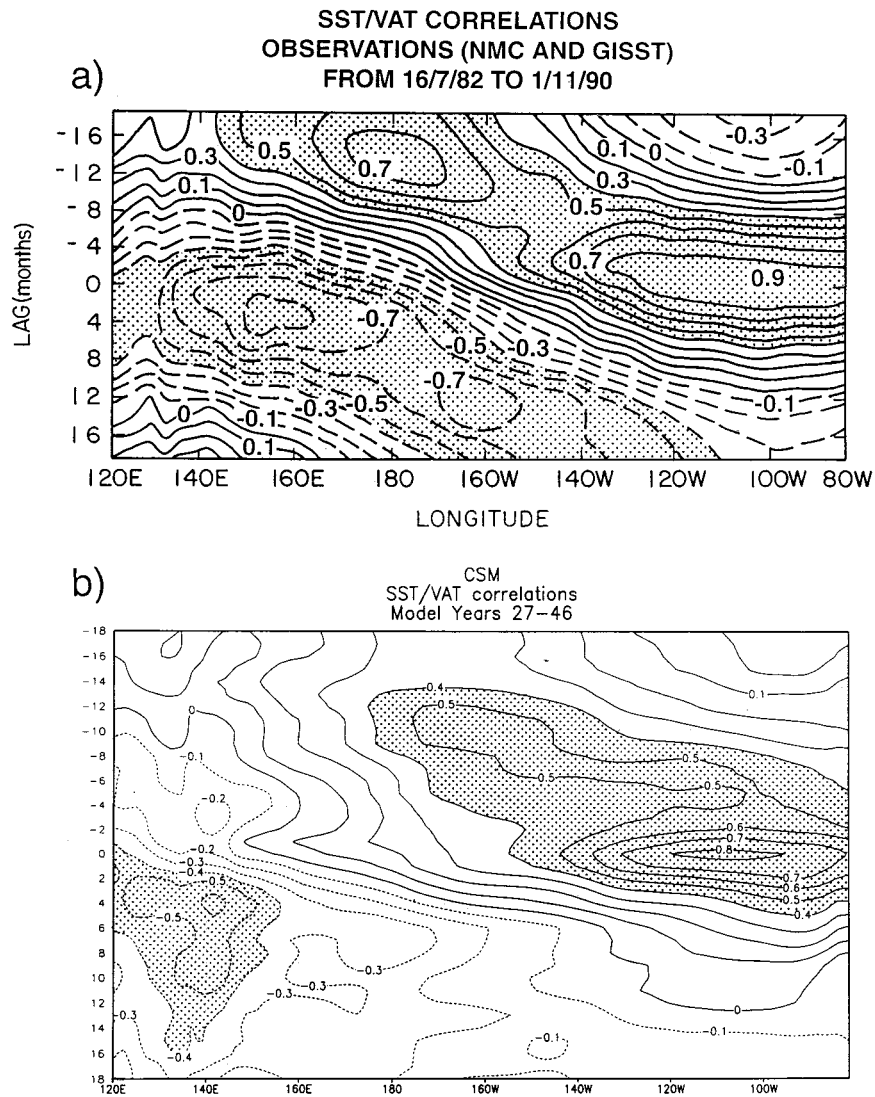
FIG. 15. Lag correlations of time series of vertically averaged temperature (VAT, temperatures averaged over the top 360 m, a measure of upper-ocean heat content) at each grid point across the Pacific averaged from 5°N to 5°S with NINO3 SST, (a) observed (1982–90 from S. Tett 1997, personal communication) and (b) CSM. Lag correlations greater than +0.4 and less than −0.4 are stippled.

less than −0.5°C (for La Niña-like events). Using that criteria, for the 45-yr period there are five El Niño-like events and four La Niña-like events. In Figs. 16a,b, Hovmöller diagrams (averaged along the equator) of the time–longitude evolution of the composite El Niño-like events is compared to a composite of El Niño events formed for the period 1979–95 from the NCAR–NCEP reanalyses. During this time there were three El Niño events (year 0 or the year of initiation of an event): 1982, 1986, and 1991. These events did not all conform to the canonical evolution documented for earlier events (Rasmusson and Carpenter 1982; Wang 1995; Trenberth and Hoar 1996), but they do provide an indication of the general features associated with such events.

Figure 16a shows that in the year prior to the inception to an event in the observations there are negative SST anomalies east of the date line of several tenths of a degree and associated easterly 850-mb wind anomalies of about 1–2 m s⁻¹. The transition to positive anomalies greater than +0.5°C occurs first in the western Pacific early in year 0. Positive SST anomalies and westerly low-level wind anomalies become established right across the Pacific by late northern spring. There is evidence of weak westward propagation of anomalies greater than +0.5°C from the eastern to central Pacific in northern summer to northern winter of year 0 [seen more strongly in the pre-1982 events as shown by Rasmusson and Carpenter (1982)], with peak anomalies ex-
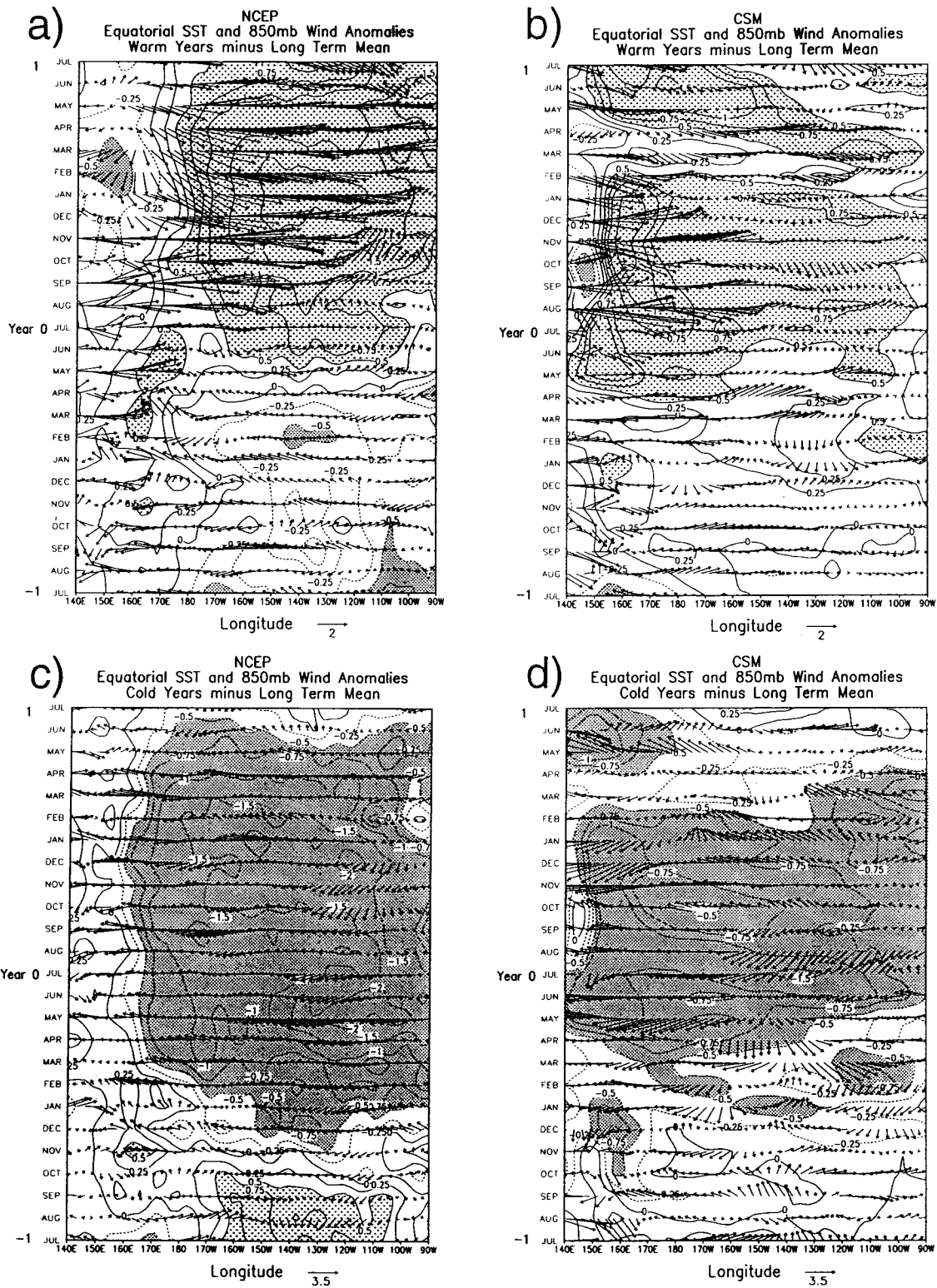
FIG. 16. (a) Hovmöller diagram of monthly anomalies of SST and 850-mb vector wind for composite ENSO warm events from NCAR–NCEP reanalysis for years 0 of 1982, 1986, and 1991, vector scaling arrow (m s⁻¹) at bottom of frame; (b) same as (a) except for composite ENSO warm events from CSM (5 years 0 defined as the first year the NINO3 SST anomaly in Fig. 8 rises above +0.5°C); (c) same as (a) except for composite La Niña cold events for years 0 of 1985 and 1988; (d) same as (b) except for composite La Niña cold events from CSM (4 years 0 defined as the first year the NINO3 SST anomaly in Fig. 8 goes below −0.5°C). Dark stippling indicates areas less than −0.5°C, light stippling areas greater than +0.5°C.

ceeding $+2.0°C$ and $+4$ m s^{-1}. The characteristic multiyear events of the 1980s and 1990s (Wang 1995; Trenberth and Hoar 1996) are evidenced by a continuation of the positive SST anomalies through northern summer of year $+1$. Events from the pre-1980 period tended to terminate in northern spring of year $+1$ (Rasmusson and Carpenter 1982; Meehl 1987, 1990).

For the CSM in Fig. 16b, there is a multiyear character to the anomalies such that positive SST anomalies of about $+0.5°C$ and westerly wind stress anomalies nearly all the way across the Pacific with values of around 2 m s^{-1} appear in northern spring of year 0, similar to the observations in Fig. 16a. The largest anomalies in excess of $+1.5°C$ and $+4$ m s^{-1} occur in the western Pacific compared to similar magnitude anomalies in the eastern Pacific in the observations. In the CSM in Fig. 16b there is a secondary pulse of positive SST anomalies and westerly wind stress anomalies in northern spring of year $+1$ that carries the composite events on into a second year.

For the La Niña or cold events, observations in Fig. 16c (for years 0 of 1985 and 1988) show similar features to the El Niño events in Fig. 16a but with signs reversed. Thus, there are positive SST anomalies the year prior to an event associated with westerly low-level wind anomalies. Easterly wind anomalies spreading from east to west early in year 0 (with a somewhat earlier onset than the positive SST anomalies during El Niño events in Fig. 16a) are associated with the negative SST anomalies. Peak values of anomalies during the second half of year 0 east of the date line exceed $-1.5°C$ and -4 m s^{-1}. SST anomalies less than $-0.5°C$ are terminated late in northern spring of year $+1$.

For the CSM La Niña-like events in Fig. 16d , multiyear aspects of the El Niño-like events in Fig. 16b are also evident. Easterly low-level wind anomalies and negative SST anomalies appear across the Pacific in northern autumn of year -1; SST anomalies less than $-0.5°C$ become established across the Pacific during northern spring of year 0 as in the observations; peak anomalies in excess of $-1.5°C$ and -4 m s^{-1} are evident during the second half of year 0 in the western Pacific compared to the eastern Pacific in the observations; and disappearance of SST anomalies less than $-0.5°C$ occurs in northern spring. A secondary pulse (as in Fig. 16b) of negative SST anomalies and easterly low-level wind anomalies is present and can be followed from the eastern Pacific in February $+1$ to the western Pacific in June $+1$, though it is not as well defined as in the El Niño-like events in Fig. 16b. In general, the seasonal timing and evolution of the events in the CSM resembles many aspects of the observed composite events, with the biggest discrepancies occurring in the western Pacific in the CSM where largest-amplitude anomalies occur, compared to the eastern Pacific in the observations.

Geographical distributions of surface temperature, precipitation, SLP, and 850-mb winds for El Niño minus La Niña events defined above for the observations are shown for the northern summer (JJA) season of year 0 in Fig. 17. Largest amplitude SST anomalies are evident in the far eastern equatorial Pacific with differences exceeding $+1.5°C$ (Fig. 17a). Positive precipitation anomalies in Fig. 17b extend right across the equatorial Pacific, with suppressed precipitation (negative anomalies) over many regions of Australasia. However, the anomalies are small over India itself. Negative SLP differences cover most of the Pacific, with largest values in excess of -2 mb in the subtropics of both hemispheres, while small-amplitude positive SLP differences cover much of Australasia (Fig. 17c). The 850-mb vector wind differences show westerly anomalies over most of the western Pacific warm pool and no clearly defined anomaly pattern in the Indian sector.

For the CSM in Fig. 18 (as indicated in the Hovmöller diagrams in Fig. 17), the largest-amplitude positive SST anomalies are established in the western Pacific (values exceeding $+1.5°C$) with negative differences of around $-0.5°C$ in the northwest and southwest Pacific. Positive precipitation anomalies are also greatest in the western Pacific in Fig. 18b, with negative differences over much of Australasia. SST anomalies in the CSM in Fig. 18a are near zero off the west coast of South America near the equator, while observed SST anomalies in that location in Fig. 17a are greater than 1°C. Though attribution of these features to specific causes is beyond the scope of this paper, we speculate that simulation features involving both the seasonal cycle (Figs. 6–7) and interannual variability (e.g., Figs. 16–18) are in general problematic for the CSM and the other coupled models as well (Mechoso et al. 1995). This could relate to errors in the mean wind field (Fig. 2) or in other coupled processes in that region (Neelin and Dykstra 1995).

Negative SLP differences (Fig. 18c) cover most of the Pacific as in the observations, with larger-amplitude negative difference maxima in the Pacific displaced somewhat poleward near 40°N and 40°S compared to 30°N and 30°S in the observations in Fig. 17c. Small-amplitude positive differences of around 1 mb cover most of Australasia. Stronger than observed westerly wind anomalies (about 7–8 m s^{-1} in the CSM compared to 5–6 m s^{-1} in the observations) occur in the western equatorial Pacific in the CSM, with easterly component vector wind differences over the Arabian Sea (associated with the suppressed precipitation over south Asia in Fig. 18b) indicative of the strong inverse relationship between tropical Pacific SSTs and the Indian monsoon in the CSM noted above in Figs. 10 and 11.

For the following northern winter (DJF) season in Fig. 19, the El Niño minus La Niña differences for observations show positive SST differences with largest values east of the date line (over $+2.5°C$) and negative differences to the north and south in the subtropics of the Pacific. Associated with these SST differences, there are positive precipitation anomalies in the central equatorial Pacific with values in excess of 12 mm day^{-1} and suppressed precipitation (negative differences) over
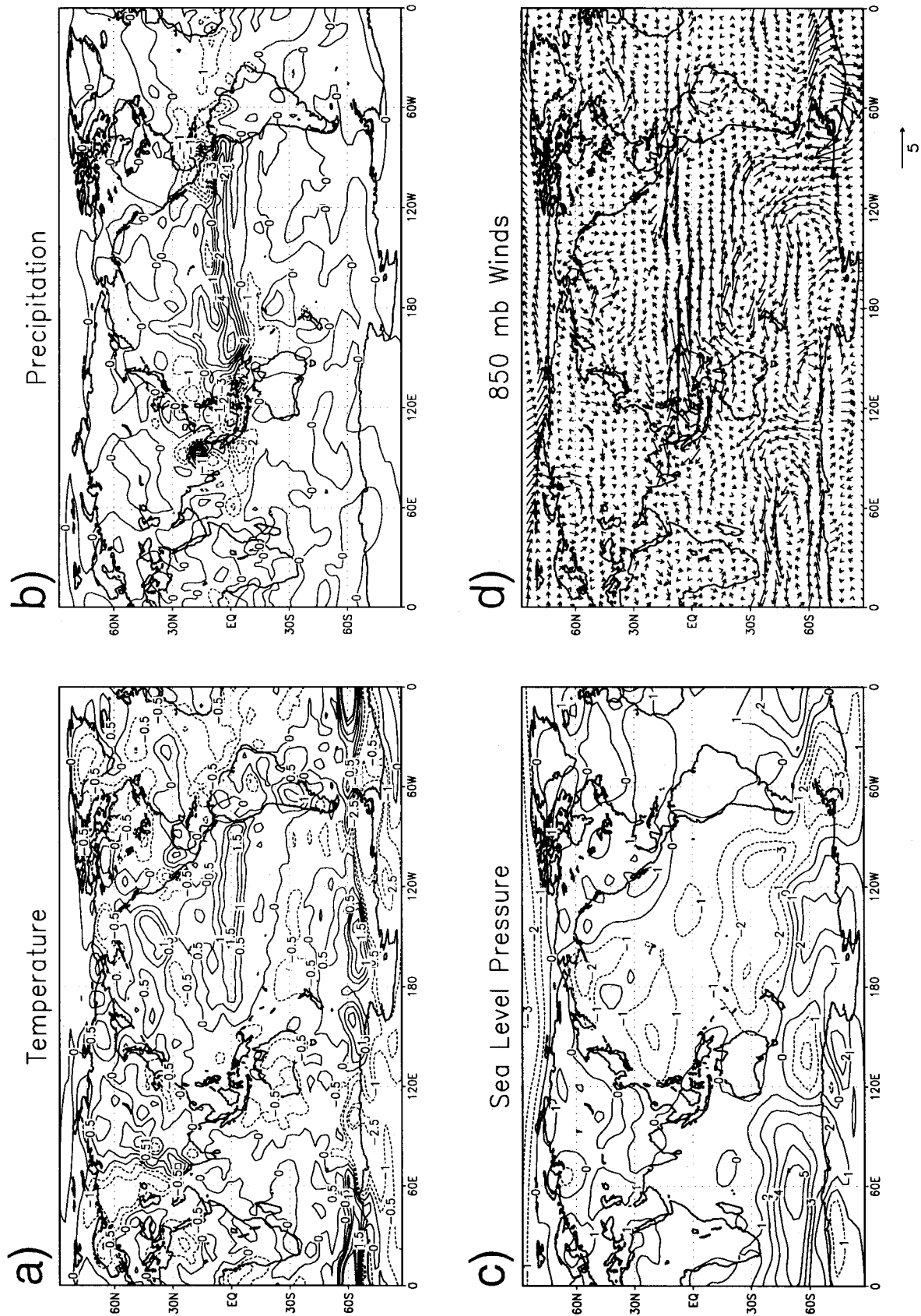
Fig. 17. Using the same composite ENSO warm events in Fig. 16, observed anomalies from the NCAR–NCEP reanalyses and Xie and Arkin (1996) are for JJA of year 0 for (a) surface temperature, (b) precipitation, (c) sea level pressure, and (d) 850-mb vector winds.
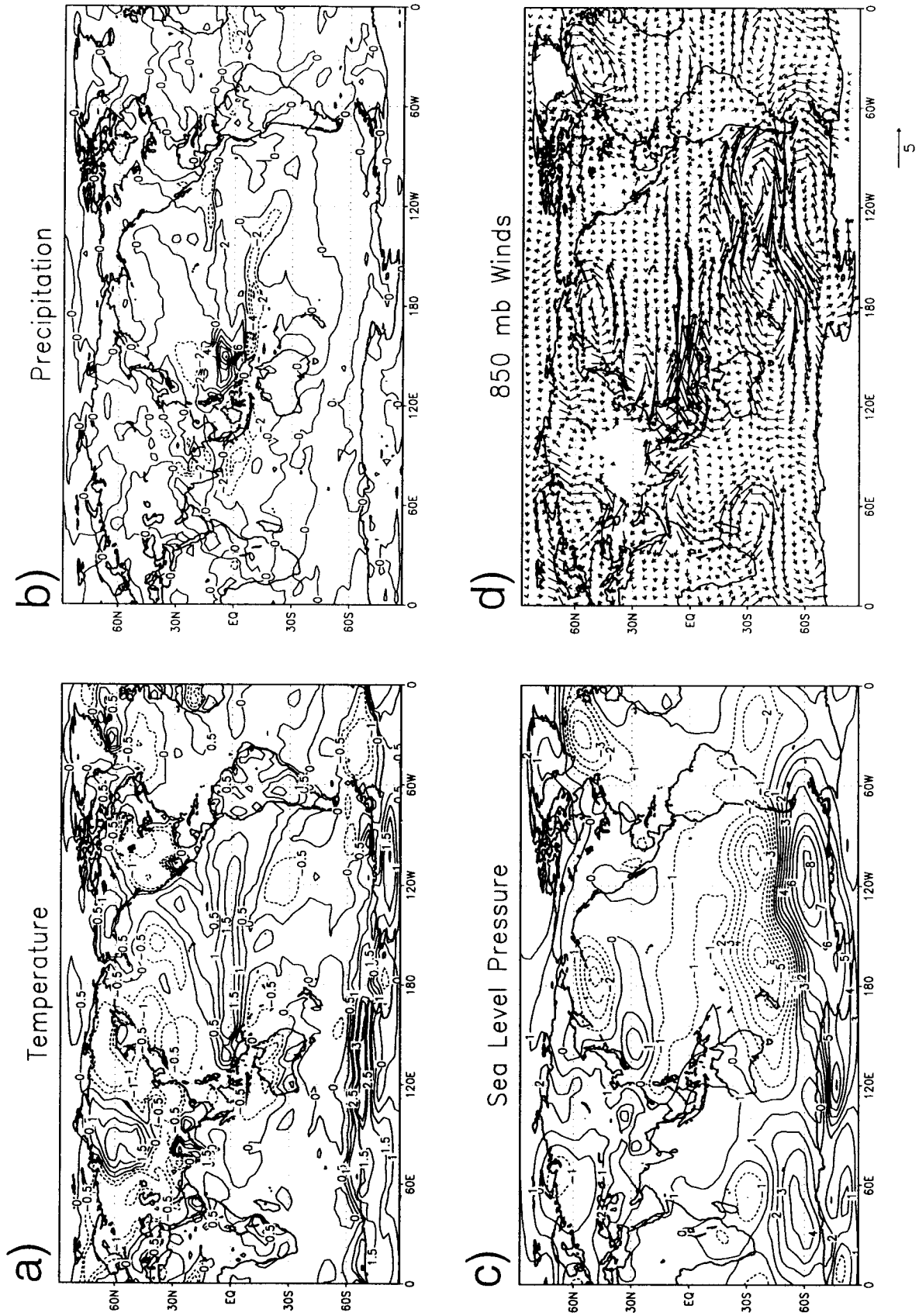
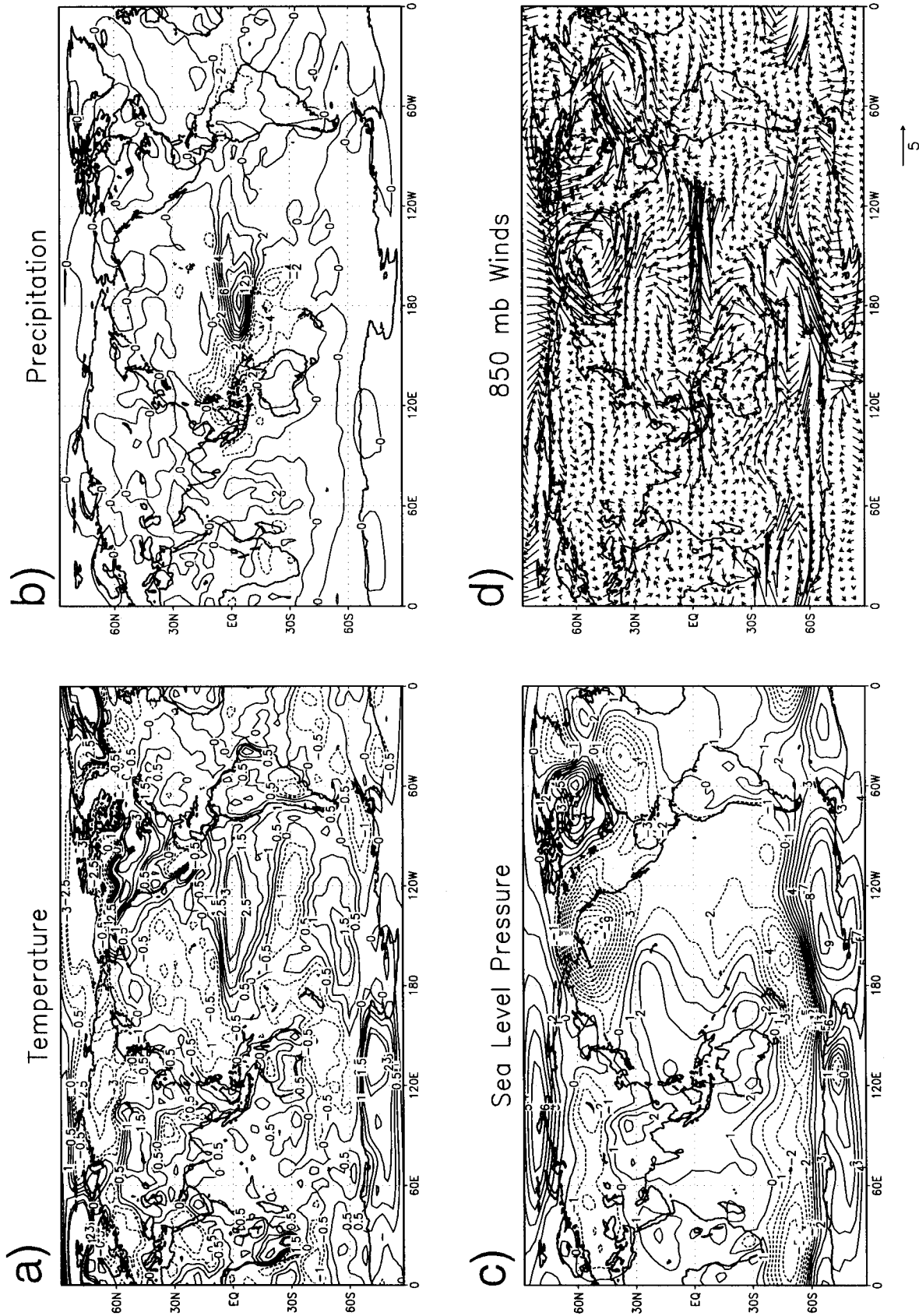FIG. 18. Same as Fig. 17 except for the five composite ENSO warm events from the CSM.

FIG. 19. Same as Fig. 17 except for the composite La Niña cold events for DJF of year 0 into year +1.

southeast Asia to the west. SLP differences in Fig. 19c show a strong Southern Oscillation pattern with negative values of 1–2 mb over the eastern tropical Pacific and positive differences of similar magnitude over Australasia. An enhanced Aleutian low, in this case represented by negative differences over −10 mb in the Gulf of Alaska, is associated with negative differences of several mb in the southern midlatitudes near 50°S across the southwest Pacific and Indian Oceans. The 850-mb wind differences in Fig. 19d show westerly vector wind anomalies of 7–8 m s^{-1} across most of the central equatorial Pacific and easterly anomalies to the west over Southeast Asia.

The CSM in Fig. 20 shows qualitatively similar features to the observations in the large-scale patterns, with some regional differences. The largest-amplitude positive SST differences in Fig. 20a are centered near 160°E in the western Pacific compared to the observations that had largest values east of the date line. Associated with those SST differences, the largest positive precipitation differences in the CSM in Fig. 20b are over the western Pacific warm pool, while they are centered near the date line in the observations in Fig. 19b. SLP differences in the CSM are around −0.5 mb over the eastern equatorial Pacific in Fig. 20c, while they exceed +3 mb over the Indian Ocean. In the observations in Fig. 19c, the negative SLP anomalies in the eastern Pacific are about twice those in the CSM, while the positive differences in the Indian sector are about half that of the CSM. The deepened Aleutian low in the north Pacific in the CSM is present in Fig. 20c as represented by maximum negative SLP anomalies of about −11 mb but shifted south and centered near 45°N (as opposed to about 60°N in the observations). The negative SLP differences near 50°S do not extend as far across the Indian Ocean in the CSM compared to the observations. The 850-mb vector wind differences are consistent with the SST and SLP results in that the largest-amplitude westerly anomalies (about 6–7 m s^{-1}) are centered in the western equatorial Pacific compared to the observations where they are mostly east of the date line. The easterly values in the Indian sector are also shifted west toward the equatorial western Indian Ocean.

To further illustrate the westward shift of the maximum SST variance in the CSM compared to observations, Fig. 21 shows the ratio of interannual standard deviations for the 45-yr time series of observed SSTs and those calculated from the CCM3 over land, and standard deviations of surface temperatures calculated for land and ocean from CSM. Areas greater than 1.0, indicating the CSM is simulating greater interannual variability of surface temperatures, are shaded. Note maximum values greater than 2 near the equator, 155°E in the western Pacific warm pool, consistent with the results described above in Figs. 16–20 in that the CSM is overestimating SST interannual variability in that location compared to the observations. There is also enhanced interannual variability of SSTs in the CSM ex-

tending northeastward and southeastward from the western Pacific into the subtropics of the central Pacific. These aspects of interannual SST variability are related in part to the variability of the surface winds and to the mean temperature structure in the upper ocean. Examination of upper-ocean temperature profiles (not shown) shows that the areas of enhanced SST variability in the CSM have colder than observed temperatures in the thermocline, while there are warmer than observed thermocline temperatures in the areas of reduced interannual SST variability in the eastern tropical Pacific. This implies that the cooler thermocline waters are more easily reached via Ekman pumping, thus contributing to larger SST variability, while the opposite would be the case in areas of warmer thermocline water. Additionally, in the equatorial eastern Pacific the CSM surface u wind has less interannual variability than the observations, while some areas of the western Pacific (as noted in Figs. 16–20) and in the off-equatorial tropical Pacific have enhanced surface wind variability. Of course the ocean temperatures and surface winds are closely coupled, and further sensitivity experiments are required to elucidate the exact combination of processes responsible for the patterns of SST variability in the CSM.

Though the values over ocean points are for CSM compared to observations, the values over land are indicative of the interannual variability produced in land surface temperatures in the CCM3 compared to the CSM. Most notable in this measure is enhanced variability over India in the CSM compared to the CCM3, consistent with the greater linkages between the Indian monsoon and tropical Pacific SSTs shown in Fig. 11.

7. Conclusions

This comparison between CSM and observations must not be taken too literally due to the small sample from the observations and the large interevent variability. In general, the CSM without flux adjustment is performing at a level comparable to or somewhat better than some other global coupled models in its class. Some consistent features are evident in the CSM compared to the CCM3 run with observed SSTs for the period 1950–94 and observations, and can be summarized as follows.

1) The CSM represents most major features of the tropical Pacific–Asian–Australian monsoon system climatology, with oceanic precipitation maxima greater than observed by about 50% or more and monsoon rainfall about 50% of the observed values. Largest discrepancies between the CSM, observations, and the CCM3 simulation occur in the equatorial eastern Indian Ocean and near the Philippines. Additionally, the equatorial SST gradient across the Pacific in the CSM is shown to be similar to the observed with somewhat cooler mean SSTs across the entire Pacific by about 1°–2°C.
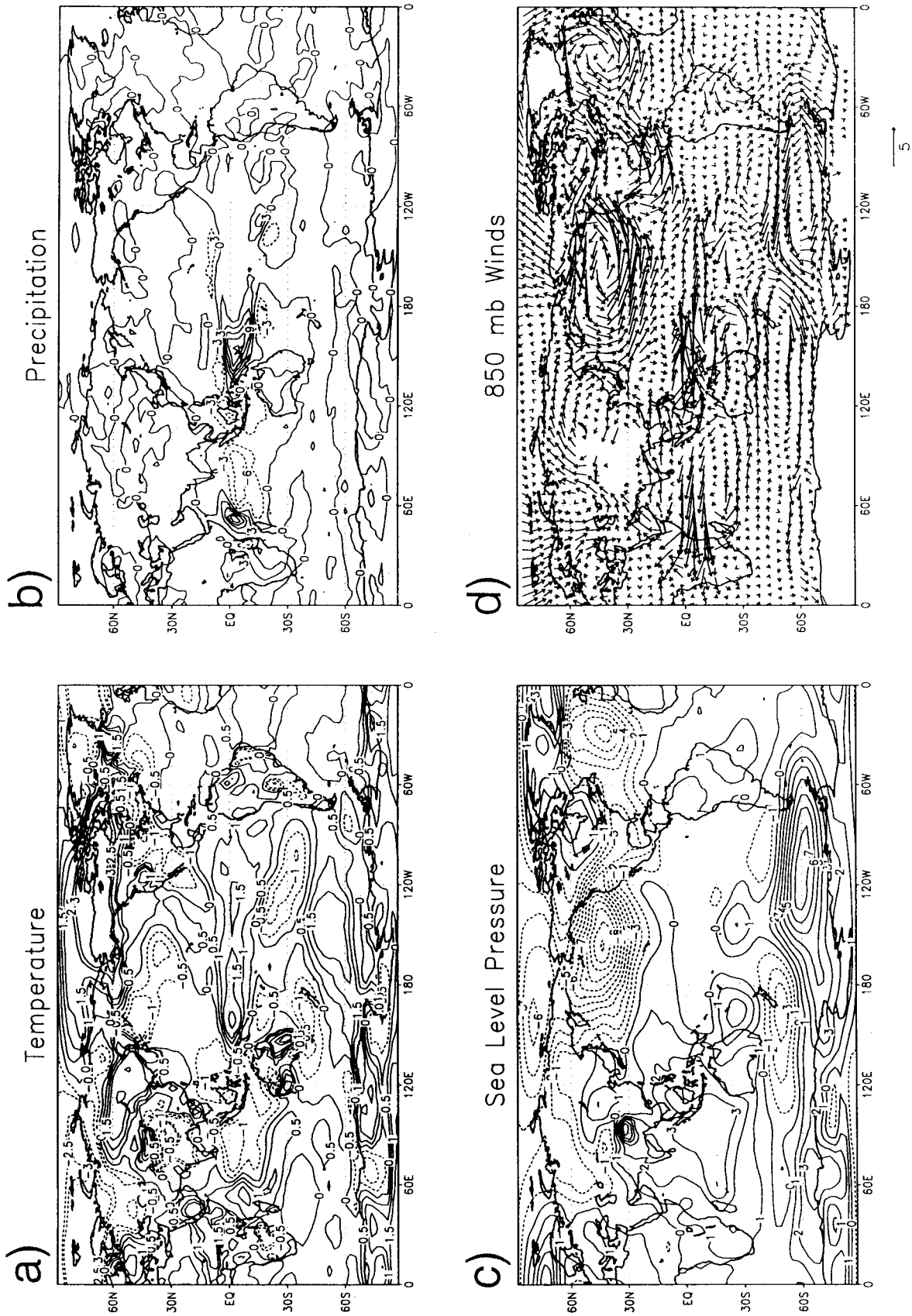
FIG. 20. Same as Fig. 18 except for the four composite La Niña cold events from the CSM.
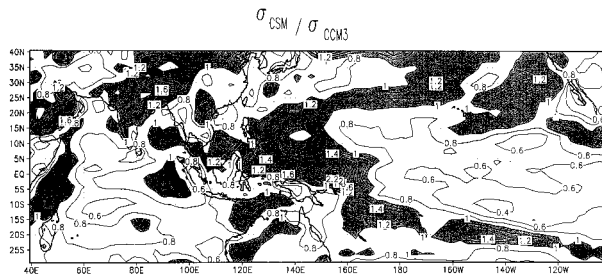
FIG. 21. Ratio of the standard deviation of annual mean surface temperature for the CSM and CCM3 45-yr integrations. Areas where the ratio exceeds 1.0 (denoting more interannual variability in the CSM compared to the observations over ocean and surface temperatures computed by the CCM3 over land) are stippled.

2) The seasonal cycle of SSTs in the eastern equatorial Pacific in the CSM has the characteristic signature seen in the observations of relatively warmer SSTs propagating westward in the first half of the year followed by the reestablishment of the cold tongue with relatively colder SSTs propagating westward in the second half of the year. Like other global coupled models, the establishment of the relatively warmer water in the first half of the year occurs about 1–2 months later than observed thus simulating a stronger semiannual component than in the observations. The seasonal cycle of precipitation in the tropical eastern Pacific is also similar to other global coupled models with this horizontal resolution in that there is a tendency for a stronger than observed double ITCZ year round but particularly in northern spring. The precipitation maximum is farther poleward by several degrees of latitude and has greater latitudinal extent but with a well-reproduced annual maximum of ITCZ strength north of the equator in the second half of the year.

3) Time series of area-averaged SSTs for the NINO3 region in the eastern equatorial Pacific show that the CSM produces about 60% of the amplitude of the observed variability in that region, consistent with most other global coupled models. Global correlations between NINO3 time series, global surface temperatures, and sea level pressure show that the CSM qualitatively reproduces the major spatial patterns associated with the Southern Oscillation (lower SLP in the central and eastern tropical Pacific when NINO3 SSTs are relatively warmer with higher SLP over the far western Pacific and Indian Oceans, with colder water in the northwest and southwest Pacific).

4) Indices of Asian–Australian monsoon strength are negatively correlated with NINO3 SSTs as in the observations. Spectra of two Indian monsoon indices and NINO3 SSTs from the CSM show coherent amplitude peaks in the Southern Oscillation and tropospheric biennial oscillation (TBO) frequencies (3–6 yr and about 2.3 yr, respectively), though only the ENSO-related peak in MCI and NINO3 SSTs is sig-

nificant at the 95% level. There is much less coherence between the Australian monsoon index and NINO3 SSTs, partly due to the westward shift of the large-scale east–west circulation in the CSM associated with colder than observed SSTs extending across the Pacific into the warm pool.

5) Lag correlations between the NINO3 SST index and upper-ocean heat content along the equator for the CSM show eastward propagation of heat content anomalies with a phase speed of about 0.3 m s^{-1}, compared to observed values of roughly 0.2 m s^{-1}. Composites of El Niño (La Niña) events in the CSM show similar seasonal evolution to composites of observed events with warming (cooling) of greater than several tenths of a degree beginning early in northern spring of year 0 and diminishing around northern spring of year +1, with a secondary resurgence later in northern spring of year +1. The CSM shows largest-amplitude ENSO SST and low-level wind variability in the western tropical Pacific, compared to the central and eastern tropical Pacific in the observations. Enhanced interannual SST variability in the CSM also extends from the western Pacific into the subtropics of the central north and south Pacific.

A number of aspects of the component models in the CSM formulation are being examined to improve features described in this paper. For example, better simulation of boundary layer stratus in the eastern Pacific should contribute to better SST simulation there. A computed cloud liquid water scheme should also contribute to improved coupled feedbacks between atmosphere and ocean. Tests are also planned with a version of the ocean model with higher latitudinal resolution in the equatorial region. This could improve the simulation of some of the ENSO phenomena documented in this study as well.

REFERENCES

Bonan, G. B., 1998: The land surface climatology of the NCAR land surface model (LSM 1.0) coupled to the NCAR Community Climate Model (CCM3). *J. Climate,* **11,** 1307–1326.

Boville, B., and P. Gent, 1998: The NCAR Climate System Model, version one. *J. Climate,* **11,** 1115–1130.

Chakraborty, B., and M. Lal, 1994: Monsoon climate and its change in a doubled CO_2 atmosphere as simulated by CSIRO9 model. *Terr. Atmos. Oceanic Sci.,* **5,** 443–464.

Dijkstra, H. A., and J. D. Neelin, 1995: Ocean–atmosphere interaction and the tropical climatology. Part II: Why the Pacific cold tongue is in the east. *J. Climate,* **8,** 1343–1359.

Gent, P., F. Bryan, G. Danabasoglu, S. Doney, W. Holland, W. Large, and J. McWilliams, 1998: The NCAR Climate System Model global ocean component. *J. Climate,* **11,** 1287–1306.

IPCC, 1996: *Climate Change 1995: The Science of Climate Change.* Cambridge University Press, 572 pp.

Ju, J., and J. Slingo, 1995: The Asian summer monsoon and ENSO. *Quart. J. Roy. Meteor. Soc.,* **121,** 1133–1168.

Kiehl, J. T., J. J. Hack, G. Bonan, B. Boville, D. Williamson, and P. Rasch, 1998: The National Center for Atmospheric Research Community Climate Model: CCM3. *J. Climate,* **11,** 1131–1149.

Kiladis, G. N., and H. van Loon, 1988: The Southern Oscillation. Part VII: Meteorological anomalies over the Indian and Pacific sectors associated with the extremes of the oscillation. *Mon. Wea. Rev.,* **116,** 120–136.

Kitoh, A., 1992: Simulated interannual variations of the Indo–Australian monsoons. *J. Meteor. Soc. Japan,* **70,** 563–583.

Knutson, T. R., and S. Manabe, 1994: Impact of increased CO_2 on simulated ENSO-like phenomena. *Geophys. Res. Lett.,* **21,** 2295–2298.

——, ——, and D. Gu, 1997: Simulated ENSO in a global coupled ocean–atmosphere model: Multidecadal amplitude modulation and CO_2 sensitivity. *J. Climate,* **10,** 138–161.

Krishnamurti, T. N., H. S. Bedi, and M. Subramanian, 1989: The summer monsoon of 1987. *J. Climate,* **2,** 321–340.

——, ——, and ——, 1990: The summer monsoon of 1988. *Meteor. Atmos. Phys.,* **42,** 19–37.

Lal, M., U. Cubasch, and B. D. Santer, 1994: Effect of global warming on Indian monsoon simulated with a coupled ocean–atmosphere general circulation model. *Curr. Sci.,* **66,** 430–438.

Laprise, R., 1992: The resolution of global spectral models. *Bull. Amer. Meteor. Soc.,* **73,** 1453–1454.

Latif, M., A. Sterl, M. Assenbaum, M. M. Junge, and E. Maier-Reimer, 1994: Climate variability in a coupled GCM. Part II: The Indian Ocean and monsoon. *J. Climate,* **7,** 1449–1462.

Lau, K.-M., and P. J. Sheu, 1988: Annual cycle, quasi-biennial oscillation, and Southern Oscillation in global precipitation. *J. Geophys. Res.,* **93,** 10 975–10 988.

Lau, N.-C., S. G. H. Philander, and M. J. Nath, 1992: Simulation of ENSO-like phenomena with a low-resolution coupled GCM of the global ocean and atmosphere. *J. Climate,* **5,** 284–307.

Ma, C.-C., C. R. Mechoso, A. W. Robertson, and A. Arakawa, 1996: Peruvian stratus clouds and the tropical Pacific circulation: A coupled ocean–atmosphere GCM study. *J. Climate,* **9,** 1635–1645.

Mechoso, C. R., and Coauthors, 1995: The seasonal cycle over the tropical Pacific in general circulation models. *Mon. Wea. Rev.,* **123,** 2825–2838.

Meehl, G. A., 1987: The annual cycle and interannual variability in the tropical Pacific and Indian Ocean regions. *Mon. Wea. Rev.,* **115,** 27–50.

——, 1990: Seasonal cycle forcing of El Niño–Southern Oscillation in a global coupled ocean–atmosphere GCM. *J. Climate,* **3,** 72–98.

——, 1994: Coupled land–ocean–atmosphere processes and south Asian monsoon variability. *Science,* **266,** 263–267.

——, 1995: Global coupled general circulation models. *Bull. Amer. Meteor. Soc.,* **76,** 951–957.

——, 1997a: The south Asian monsoon and the tropospheric biennial oscillation. *J. Climate,* **10,** 1921–1943.

——, 1997b: Modification of surface fluxes from component models in global coupled models. *J. Climate,* **10,** 2811–2825.

——, and W. M. Washington, 1993: South Asian summer monsoon variability in a model with doubled atmospheric carbon dioxide concentration. *Science,* **260,** 1101–1104.

——, G. W. Branstator, and W. M. Washington, 1993a: Tropical Pacific interannual variability and CO_2 climate change. *J. Climate,* **6,** 42–63.

——, W. M. Washington, and T. R. Karl, 1993b: Low-frequency variability and CO_2 transient climate change. Part 1: Time-averaged differences. *Climate Dyn.,* **8,** 117–133.

——, M. Wheeler, and W. M. Washington, 1994: Low-frequency variability and CO_2 transient climate change. Part 3: Intermonthly and interannual variability. *Climate Dyn.,* **10,** 277–303.

Nagai, T., T. Tokioka, M. Endoh, and Y. Kitamura, 1992: El Niño–Southern Oscillation simulated in an MRE atmosphere–ocean coupled general circulation model. *J. Climate,* **5,** 1202–1233.

Neelin, J. D., and H. A. Dijkstra, 1995: Ocean–atmosphere interaction and the tropical climatology. Part I: The dangers of flux correction. *J. Climate,* **8,** 1325–1342.

Nicholls, N., 1984: The Southern Oscillation and Indonesia sea surface temperature. *Mon. Wea. Rev.,* **112,** 424–432.

Palmer, T. N., C. Brankovic, P. Viterbo, and M. J. Miller, 1992: Modeling interannual variations of summer monsoons. *J. Climate,* **5,** 399–417.

Parthasarathy, B., K. Rupa Kumar, and A. A. Munot, 1991: Evidence of secular variations in Indian monsoon rainfall–circulation relationships. *J. Climate,* **4,** 927–938.

Rasmusson, E. M., and T. H. Carpenter, 1982: Variations in tropical sea surface temperature and surface wind fields associated with the Southern Oscillation/El Niño. *Mon. Wea. Rev.,* **110,** 354–384.

Roeckner, E., J. M. Oberhuber, A. Bacher, M. Christoph, and I. Kirchner, 1996: ENSO variability and atmospheric response in a global coupled atmosphere–ocean GCM. *Climate Dyn.,* **12,** 737–754.

Ropelewski, C. F., M. S. Halpert, and X. Wang, 1992: Observed tropospheric biennial variability and its relationship to the Southern Oscillation. *J. Climate,* **5,** 594–614.

Shea, D. J., K. E. Trenberth, and R. W. Reynolds, 1990: A global monthly sea surface temperature climatology. NCAR Tech. Note NCAR/TN-345+STR, 167 pp. [Available from NCAR, P. O. Box 3000, Boulder, CO 80307.]

Shukla, J., 1987: Interannual variability of monsoons. *Monsoons,* J. S. Fein and P. L. Stephens, Eds., John Wiley and Sons, 399–464.

Sperber, K. R., and T. N. Palmer, 1996: Interannual tropical rainfall variability in general circulation model simulations associated with the Atmospheric Model Intercomparison Project. *J. Climate,* **9,** 2727–2750.

Tett, S., 1995: Simulation of El Niño–Southern Oscillation-like variability in a global AOGCM and its response to CO_2 increase. *J. Climate,* **8,** 1473–1502.

Trenberth, K. E., and T. J. Hoar, 1996: The 1990–1995 El Niño–Southern Oscillation event: Longest on record. *Geophys. Res. Lett.,* **23,** 57–60.

Wang, B., 1995: Interdecadal changes in El Niño onset in the last four decades. *J. Climate,* **8,** 267–285.

Weatherly, J. W., B. P. Briegleb, W. G. Large, and J. A. Maslanik, 1998: Sea ice and polar climate in the NCAR CSM. *J. Climate,* **11,** 1472–1486.

Webster, P. J., and S. Yang, 1992: Monsoon and ENSO: Selectively interactive systems. *Quart. J. Roy. Meteor. Soc.,* **118,** 877–926.

Williamson, D. L., J. T. Kiehl, and J. J. Hack, 1995: Climate sensitivity of the NCAR Community Climate Model (CCM2) to horizontal resolution. *Climate Dyn.,* **11,** 377–398.

Xie, P., and P. A. Arkin, 1996: Analyses of global monthly precipitation using gauge observations, satellite estimates, and numerical model predictions. *J. Climate,* **9,** 840–858.

Yasunari, T., and Y. Seki, 1992: Role of the Asian monsoon on the interannual variability of the global climate system. *J. Meteor. Soc. Japan,* **70,** 177–189.

Yukimoto, S., M. Endoh, Y. Kitamura, A. Kitoh, T. Motoi, A. Noda, and T. Tokioka, 1996: Interannual and interdecadal variabilities in the Pacific in an MRI coupled GCM. *Climate Dyn.,* **12,** 667–683.